A phase field approach enhanced with a cohesive zone model for modeling delamination induced by matrix cracking

A. Quintanas-Corominas[a], A. Turon[a], J. Reinoso[b], E. Casoni[c], M. Paggi[d], J.A. Mayugo[a]

[a] *AMADE, Polytechnic School, Universitat de Girona, Campus Montilivi s/n, 17071 Girona, Spain*
[b] *Elasticity and Strength of Materials Group, School of Engineering, Universidad de Sevilla, Camino de los Descubrimientos s/n, 41092, Seville, Spain*
[c] *Barcelona Supercomputing Center (BSC-CNS), Edificio NEXUS I, Campus Nord UPC, Gran Capitán 2–4, 08034, Barcelona, Spain*
[d] *IMT School for Advanced Studies Lucca, Piazza San Francesco 19, 55100, Lucca, Italy*

Abstract

The progressive damage analysis of fibre-reinforced composite materials is a challenging task, especially when complicated cracking scenarios arise due to the onset and progression of several damage mechanisms. From a modelling point of view, a particularly complex failure scenario is the interaction between intralaminar and interlaminar cracks. This work proposes a novel framework accounting for this interaction through the coupling of a nonlocal damage model based on the phase field approach for the intralaminar failure with a cohesive zone model for the interlaminar one. The modular variational formalism of the method presented leads to a very compact and efficient numerical strategy, which endows the fulfillment of the thermodynamic consistency restrictions and provides a relatively simple basis for its finite element implementation due to the preclusion of complex crack tracking procedures with standard element architectures. After addressing its implementation in the context of the finite element method in a High Performance Computing environment, the capabilities of the proposed formulation are explored through a numerical investigation of a cross-ply laminate subjected to a 4-point bending configuration. The comparison of the numerical predictions against the experimental observations demonstrates the reliability of the proposed framework for capturing the delamination induced by matrix cracking failure scenario.

Keywords: A. Composite materials; B. FE-modeling; C. Damage modeling; D. Fracture; E. Interlaminar

1. Introduction

Long Fiber-Reinforced Composites (LFRC) laminates proportionate a well-suited option for light-weight applications thanks to their excellent specific strength and stiffness ratios. The intricate and heterogeneous internal arrangement of these materials provides their strengths but also hinds the prediction of their bearing capacities. The principal reason that difficults the estimation of the bearing capacities is becouse the failure process of a LFRC laminates can be driven by several damage mechanisms which, moreover, can interact between them. For this reason, a Progressive Damage Analysis (PDA) is normally necessary to predict under arbitrary loading conditions the bearing capacities of a LFRC structure. At the mesoscopic level, a PDA of LFRC laminates needs to model the mechanical response of two clearly differentiated regions: the intralaminar that refers to the region inside a ply and the interlaminar that refers to the region between two adjacent plies, which is named interface.

In the context of Finite Element Method (FEM), a commonly-adopted strategy for performing PDFA of LFRC on the mesoscopic level is to model the intralaminar and interlaminar regions independently. Hence, different models are employed without a direct coupling between the failure events occurring in both regions. Following this strategy, local Continuum Damage Models (CDMs) have been extensively used for capturing the intralaminar damage mechanisms, namely: breaking and kinking of the fibers and cracking of the matrix [1, 2, 3, 4]. In turn, Cohesive Zone Models (CZMs) have been successfully employed for

describing the main interlaminar damage, the so-called interface debonding or delamination [5, 6, 7, 8]. Despite the excellent results [9, 10, 11, 12], this strategy has some flaws that arise from the local character of the models. On the one hand, the local CDMs suffer from localization problems due to the loss of the ellipticity of the governing equations, which leads to mesh-dependent results [13]. On the other hand, the local character of formulations makes difficult the interchanges of information regarding the damage state between both regions. This interchange can be essential to model complex failure scenarios, such as the case of delamination induced by transverse cracks.

In the last decades, the Phase Field (PF) approach to brittle fracture has emerged as a reliable alternative beyond the classical nonlocal CDMs for modeling progressive failure events without the aforementioned localization issue. The PF approach, in essence, is a regularization strategy of the variational problem for the brittle fracture proposed by Francfort and Marigo [14]. After the pioneering work of Bourdin et al. [15, 16] and later of Miehe et al. [17], the PF approach has been used to model the onset and progression of different types of fractures: (i) brittle [18, 19, 20, 21], (ii) ductile [22, 23, 24, 25], (iii) hydraulic and hydrogen driven [26, 27], (v) thermo-elastic–plastic [28, 29, 30], and (v) anisotropic behaviors [31, 32, 33, 34, 35, 36, 37].

Despite the potential of PF approach, few works have addressed their application for modelling the failure of composite materials. For instance, Reinoso et al. [38] successfully predicted the failure of thin-ply laminates by combining the PF with a continuum shell theory. Later, Alessi and Fredi [25] proposed a one-dimensional PF model to predict the failure of unidirectional hybrid laminates under uniaxial loading conditions. Subsequently, Bleyer and Alessi [39] extended their approach to a multi-dimensional model that employs several PFs to account for the failure induced by the fibre breaking and matrix cracking separately. In line with the previous approach, Quintanas-Corominas et al. [40] presented a formulation to model the anisotropic mechanical response of LFRC using a single damage-type variable. In this last study, they demonstrated the capabilities of their formulation by making a comparison of the intralaminar and translaminar failure predictions against the most common modeling approaches: LEFM, CDM, and CZM.

The existence of interfaces make difficult the employment of the PF approach via a physically sound variational formalism. To overcome this issue, Paggi and Reinoso [41] recently presented an approach that combines the PF approach for the bulk region with a CZM for the interface one. In this sense, they proposed a physically consistent strategy to couple via the PF variable a tension cut-off interface behavior with the damage state of the surrounding bulk region by reducing the apparent stiffness of the interface as the PF increases. This hypothesis is suitable for relatively brittle interface behavior as they demonstrated in several studies: (i) layered ceramics [42, 43], (ii) micro-mechanics of poly-crystalline [44], and (iii) micro-mechanics of FRC [45].

This work aims to present a PF-CZM approach for modeling the interaction between the intralaminar and interlaminar damage mechanisms, constituting an alternative to the classical CDM-CZM approaches [46]. The main innovative aspects herein presented are: (i) the usage of the PF model proposed by Quintanas-Corominas et al. [40] for the intralaminar failure events and the CZM proposed by Turon et al. [47] for the interlaminar one, (ii) the coupling strategy between both constitutive models via the PF variable, and (iii) the numerical implementation in a high-performance computing (HPC) simulation code. Indeed, it is presented a new interface model that attempts to provide a more general scenario for progressive damage model of solids with internal interfaces suitable for brittle and cohesive responses. After addressing the verification of the numerical implementation through mode-I and mode-II delamination tests, a thorough analysis of a cross-ply LFRC laminate subjected to a 4-Point Bending Test (4PBT) configuration is performed. The comparison between the numerical predictions and experimental observations demonstrate the capabilities of the presented PF-CZM approach to capture the main behavior on such complex failure scenario as the delamination induced by matrix cracking.

The manuscript is organized as follows. Section 2 briefly outlines the fundamental theoretical and numerical aspects of the PF-CZM approach. The constitutive assumptions regarding the bulk and interface regions are presented in Section 3. Section 4 introduces the implementation and applicability of the proposed formulation. In particular, the High Performance Computing (HPC) environment is environment employed is outlined in Section 4.1, while, in Section 4.3, the numerical study of the 4PBT is conducted, demonstrating predictive capabilities in very satisfactory agreement with the experimental observations. Finally, the main conclusions are summarized in Section 5.

2. Phase Field approach to fracture

This section outlines the fundamental aspects of the current modeling framework, In particular, the present methodology is derived by taking the formulation of Paggi and Reinoso [41] as the fundamental result, which sets the basis for the combination of the PF approach for bulk fracture with a consistent interface formulation relying on the cohesive-like approach. Along these lines, the variational form of the internal energy functional of a general cracked body with internal interfaces is described in Section 2.1, while the weak and discrete form of the energy functional are summarized in Sections 2.2 and 2.3, respectively.

2.1. Modeling hypotheses and variational formalism

As stated above, combining the PF and CZM methods for fracture in heterogeneous media was intuitively motivated in different investigations [41, 48, 49]. Complying with this idea, we consider an arbitrary body in the general Euclidean space of dimension $N \in [2, 3]$. Restricting the analysis to the infinitesimal deformation setting, the body occupies the domain $\mathcal{B} \subset \mathbb{R}^N$ with the external boundary denoted as $\partial\mathcal{B} \subset \mathbb{R}^{N-1}$, whose outward normal unit vector is represented by $\boldsymbol{n}$. As illustrated in Figure 1, we postulate the existence of an internal interface Γ_{i} in the system, and a discrete cracks network Γ_{c} in the bulk. The material points within the body are identified by the individual position vectors $\boldsymbol{x} \in \mathcal{B}$, whereas the displacement field is identified by $\mathbf{u}(\boldsymbol{x}, t)$. For convenience, we define the displacement jump at the interface as the relative displacement between two homologous points, i.e. $\boldsymbol{\Delta} = \mathbf{u}_a^+ - \mathbf{u}_a^-$, denoting the difference between the kinematic field along the interface flanks Γ_{i}^+ and Γ_{i}^- (Figure 1). Finally, we assume that $\mathcal{B}$ is subjected to body forces $\boldsymbol{b}$ as well as to boundary conditions in the form of prescribed displacements ($\bar{\mathbf{u}}$ on $\partial\mathcal{B}_u$) and prescribed tractions ($\bar{\boldsymbol{t}}$ on $\partial\mathcal{B}_t$). These boundary conditions are subjected to the Neumann-Dirichlet conditions, i.e. $\partial\mathcal{B}_t \cup \partial\mathcal{B}_u = \partial\mathcal{B}$ and $\partial\mathcal{B}_t \cap \partial\mathcal{B}_u = \emptyset$.

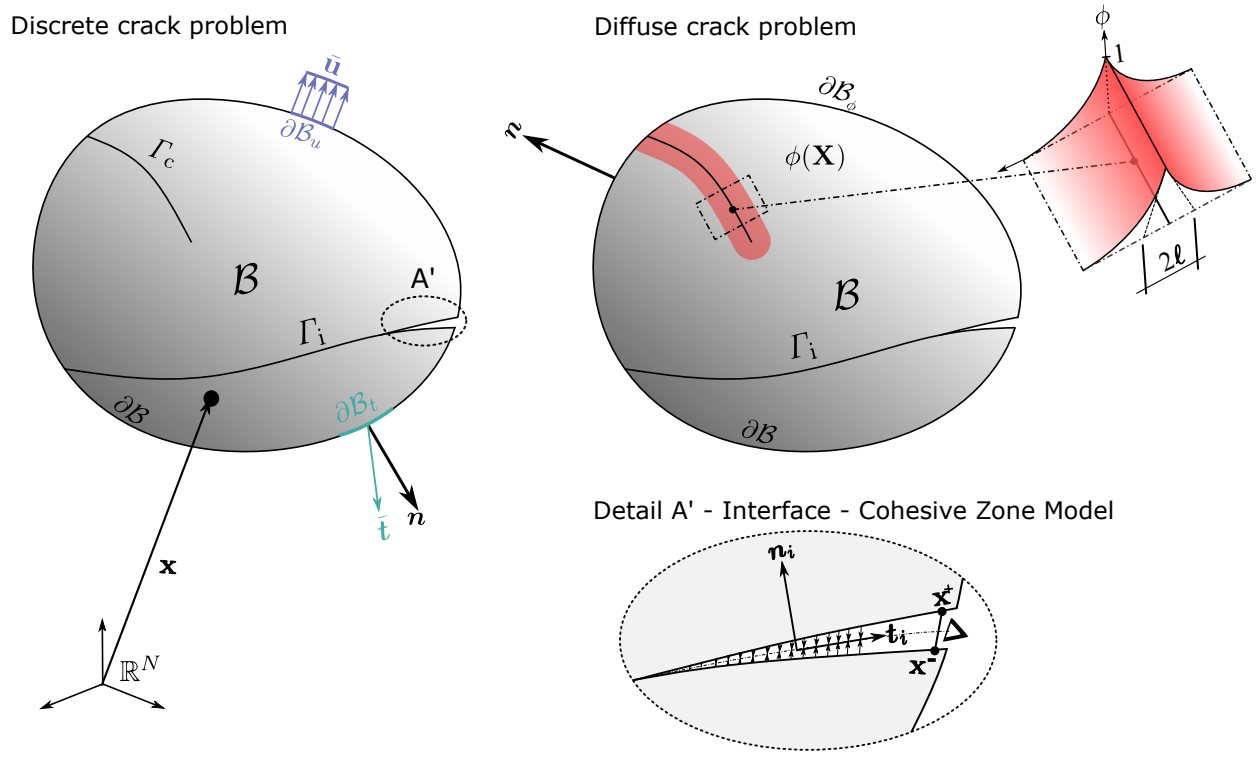

Figure 1: Schematic representation of an arbitrary body with a discontinuity in the domain and an interface.

By establishing the variational approach to fracture as the point of departure of the current formulation, it is postulated that the energy functional governing the fracture process of the system is given by

$$\Pi(\mathbf{u}, \Gamma) = \Pi_{int}(\mathbf{u}, \Gamma) - \Pi_{ext}(\mathbf{u}) \tag{1}$$

Following Bourdin et al. [15] and [41], the internal energy density functional $\Pi_{int}(\mathbf{u}, \Gamma)$ of the system under consideration can be defined as the sum of elastic energy stored in the body $\Pi_{\mathcal{B}}$ and the energy dissipated through the different potential mechanisms of fracture, i.e. bulk and interface fracture processes in the current analysis. Based on these modeling assumptions, $\Pi_{int}(\mathbf{u}, \Gamma)$ takes the particular form:

$$\Pi_{int}(\mathbf{u}, \Gamma) = \Pi_{\mathcal{B}}(\mathbf{u}) + \Pi_{\Gamma}(\Gamma), \tag{2}$$

where $\Pi_{\mathcal{B}}(\mathbf{u})$ is the energy storage function due to the deformation process of the body, and Γ is the union between the bulk and interface cracks are associated with the respectively fracture events, such that $\Gamma = \Gamma_{\mathrm{c}} \cup \Gamma_{\mathrm{i}}$. Accordingly, the fracture energy of the system can be accounted for by adding the split of the two corresponding counterparts:

$$\Pi_{int}(\mathbf{u}, \Gamma) = \Pi_{int}(\mathbf{u}, \Gamma_{\mathrm{c}}, \Gamma_{\mathrm{i}}) = \Pi_{\mathcal{B}}(\mathbf{u}) + \Pi_{\Gamma_{\mathrm{c}}}(\Gamma_{\mathrm{c}}) + \Pi_{\Gamma_{\mathrm{i}}}(\Gamma_{\mathrm{i}}) \tag{3}$$

where $\Pi_{\Gamma_{\mathrm{c}}}$ and $\Pi_{\Gamma_{\mathrm{i}}}$ are the dissipated energies that stem from the cracking events within the bulk and the debonding effects along the interfaces, respectively. Note that to evaluate the above expression, the topology of the cracks network is required. This evaluation can be very challenging due to the complex crack paths arising from the branching and coalescence phenomena, as well as the interaction with the cracks which induces the debonding processes along the existing interfaces. As proposed in [41], evaluating such complex crack patterns in heterogeneous media can be done by combining the PF approach within the bulk region and the interface elements, relying on the concept of the cohesive zone at the prescribed interfaces. In the continuation, the particular expression of the internal energy density is consistently derived but also including two new features: (*i*) the use of the recent anisotropic PF method for bulk fracture proposed in [40], and (*ii*) the consideration of cohesive-like interface crack obeying to the bilinear traction-separation law (TSL) [47].

2.1.1. Bulk region

The energy density of the bulk region Π_b includes the elastic energy stored for the body and the energy required to create and propagate the bulk cracks. Within the context of long fiber reinforced composite materials (LFRCs), these events are also known as intralaminar damage mechanisms [1, 4]. Considering the energetic criterion proposed by Griffith [50], Π_b can be defined as [15]:

$$\Pi_b(\mathbf{u}, \Gamma_{\mathrm{c}}) = \Pi_{\mathcal{B}}(\mathbf{u}) + \Pi_{\Gamma_{\mathrm{c}}}(\Gamma_{\mathrm{c}}) = \int_{\mathcal{B}\setminus\Gamma} \Psi_{\mathrm{e}}(\boldsymbol{\varepsilon}(\mathbf{u}))\, \mathrm{d}V + \int_{\Gamma_{\mathrm{c}}} \mathcal{G}_c\, \mathrm{d}S \tag{4}$$

where Ψ_{e} is the specific elastic energy function and $\mathcal{G}_{\mathrm{c}}$ is the critical energy release rate of the bulk material. The infinitesimal strain tensor $\boldsymbol{\varepsilon}$ is the symmetric gradient of the displacement field ($\boldsymbol{\varepsilon} := \nabla^s \mathbf{u}$), which is introduced here because Ψ_{e} is generally expressed with respect to the strain state.

The PF approach postulates that the discrete boundary representing a crack network Γ_{c} can be smeared over the domain $\mathcal{B}$ through the exploitation of the Γ-convergence concept [51], allowing the definition of the crack surface density functional $\gamma(\phi, \nabla\phi)$ to be defined [17]. This new functional is governed by the phase field variable ϕ and its spatial gradient $\nabla\phi$, endowing the current approach with non-local character in the spirit of gradient enhanced models [52]. Formally, the phase field variable ϕ accounts for the amount of equivalent crack surface at a material point. Therefore, in line with continuum damage mechanics (CDM) models, ϕ can be interpreted as the damage state of the material point tracking the stiffness degradation. Following the notation introduced by Miehe et al. [17], Π_b reads:

$$\Pi_b(\mathbf{u}, \Gamma_\mathrm{c}) \approx \Pi_b(\mathbf{u}, \phi) = \int_{\mathcal{B}} \Psi_\mathrm{b}(\boldsymbol{\varepsilon}(\mathbf{u}), \phi)\, \mathrm{d}V + \int_{\mathcal{B}} \mathcal{G}_\mathrm{c}\gamma(\phi, \nabla\phi)\, \mathrm{d}V \tag{5}$$

where Ψ_b is the bulk free energy functional that takes into account the degradation of elastic energy within the smearing transition zone that is characterized by ℓ, i.e. between a pristine ($\phi = 0$) and a fully-damaged ($\phi = 1$) state. It is worth mentioning that the expression of Ψ_b depends on the material model, which is presented in Section 3.1. Note that fracture toughness in Eq.(5) requires a simple modification following [16] in order to prevent the overestimation of the released energy. This modification is performed via the use of an effective energy release rate $\mathcal{G}_\mathrm{c}^\mathrm{eff}$ that depends on the spatial discretization parameter (finite element size), ℓ_e, and the phase field length scale, Ł, according to the expression: $\mathcal{G}_\mathrm{c}^\mathrm{eff} = \mathcal{G}_\mathrm{c}\left(1 - \frac{\ell_\mathrm{e}}{\ell}\right)$.

Regarding the specialization of crack density functional for intralaminar failure in LFRCs, the modified version of the Ambrosio-Tortorelli functional [51] encompassing the anisotropic character at lamina level proposed in [40] is herewith recalled:

$$\gamma(\phi, \nabla\phi) = \frac{1}{2\ell}\left(\phi^2 + \nabla\phi \cdot \boldsymbol{\mathcal{L}}\nabla\phi\right) \tag{6}$$

where $\boldsymbol{\mathcal{L}}$ is a structural tensor that aligns the phase field with a preferred direction and ℓ is the so-called length scale parameter of the PF method that controls the damage diffusion around the process region [32]. In the case of isotropic surface density, it is defined as $\boldsymbol{\mathcal{L}} = \ell^2\mathbf{I}$, whereas for an anisotropic surface this yields to $\boldsymbol{\mathcal{L}} = \ell_p^2(\mathbf{n}_p \otimes \mathbf{n}_p + \beta(\mathbf{I} - \mathbf{n}_p \otimes \mathbf{n}_p))$, where $\mathbf{n}_p$ is the principal direction vector (coinciding with the fiber direction in this work), and β is a factor governing the anisotropy [40]. As can be seen, the fracture energy contribution in Eq. (5) is integrated over $\mathcal{B}$ instead of Γ_c eliminating the explicit need to compute the crack surface topology.

2.1.2. Interface region

The energy density of the interface Π_i accounts for the debonding process along the prescribed interfaces of the system under study. This phenomenon is denominated as interlaminar damage in composite materials, which is induced by micro-cracks at the fracture process zone [53]. Differing from the previous investigations [42, 43, 41], which employed a relatively simple tension cut-off interface formulation and whose coupling with the PF method for bulk fracture regarded the modification of the interface apparent stiffness, the current method encompasses the consideration of a bilinear TSL to account for the interface debonding according to [53]. This interface model allows interlaminar failure to be triggered through a gradual stiffness reduction upon failure initiation up to the complete decohesion. Therefore, the crack opening governs the damage state at the interface, requiring the definition of an internal variable to ensure the irreversible condition of the process. In this sense, Π_i can be defined as:

$$\Pi_i(\Gamma_\mathrm{i}) \approx \Pi_i(\boldsymbol{\Delta}(\mathbf{u}), \phi) = \int_{\Gamma_\mathrm{i}} \Psi_\mathrm{i}(\boldsymbol{\Delta}(\mathbf{u}), \phi, \boldsymbol{h})\, \mathrm{d}S \tag{7}$$

where Ψ_i is the specific interface energy function. The CZM is formulated according to the continuum damage theory and, therefore, Ψ_i depends on a set of historical variables $\boldsymbol{h}$. Finally, Ψ_i incorporates the PF variable of the bulk as an additional argument, which is introduced in order to model the interaction between the bulk and interface cracks. Both Ψ_i and interaction process are presented in Section 3.2.

2.1.3. Final variational form

Relying on the previous considerations in Eq. (5) and (7), the internal energy functional of a cracked body with interfaces is herein approximated as:

$$\Pi_{int}(\mathbf{u},\Gamma) \approx \Pi_{int}(\mathbf{u},\phi) = \int_{\mathcal{B}} \left[\Psi_{\mathrm{b}}(\boldsymbol{\varepsilon}(\mathbf{u}),\phi) + \frac{\mathcal{G}_{\mathrm{c}}}{2\ell} \left(\phi^2 + \nabla\phi \cdot \boldsymbol{\mathcal{L}} \nabla\phi \right) \right] \mathrm{d}V + \int_{\Gamma_{\mathrm{i}}} \Psi_{\mathrm{i}}(\boldsymbol{\Delta}(\mathbf{u}),\phi,\boldsymbol{h}) \, \mathrm{d}S \tag{8}$$

Moreover, in the current framework, the active-passive decomposition of the bulk free energy density function is used to account for a fracture-induced stress degradation via the volumetric-deviatoric decomposition [54]:

$$\Psi_{\mathrm{b}}(\boldsymbol{\varepsilon},\phi) = \left((1-\phi)^2 + \eta_\ell \right) \Psi_{act}(\boldsymbol{\varepsilon}) + \Psi_{pas}(\boldsymbol{\varepsilon}) \tag{9}$$

where $\Psi_{e,act}$ and $\Psi_{e,pass}$ are the active and passive parts, respectively, of the elastic free energy density; and η_ℓ stands for the residual stiffness parameter to prevent numerical issues. In line with [40], we herewith adopt the previous decomposition in order to activate the driving forces for cracking evolution in the bulk under tensile load conditions (Sect. 3.1). Thus, through the use of this decomposition, the phase field only affects the so-called active term, allowing the crack closure under loading reversal to be modelled.

2.2. Weak form

Recalling the standard continuous Bubnov-Galerkin method [55], the two primary fields, $\mathbf{u}$ and ϕ, are extended with the corresponding admissible test function, $\delta\mathbf{u}$ and $\delta\phi$. Thus, the weak form of the governing functional can be constructed by its first variation with respect to the primary fields mentioned above:

$$\delta\Pi(\mathbf{u},\delta\mathbf{u},\phi,\delta\phi) = \delta\Pi_{int}(\mathbf{u},\delta\mathbf{u},\phi,\delta\phi) - \delta\Pi_{ext}(\mathbf{u}), \quad \forall\delta\mathbf{u} \in \mathcal{V}_u, \quad \forall\delta\phi \in \mathcal{V}_\phi \tag{10}$$

where $\delta\Pi_{int}$ and $\delta\Pi_{ext}$ are respectively the internal and external variations. Here, $\mathcal{V}_u = \{\delta\mathbf{u} \in \mathrm{H}^1 | \delta\mathbf{u} = 0 \text{ on } \partial\mathcal{B}_u\}$ and $\mathcal{V}_\phi = \{\delta\phi \in \mathrm{H}^1 | \delta\phi = 0 \text{ on } \Gamma_{\mathrm{c}}\}$ are the functional spaces of the admissible test functions [42, 21].

Focusing on the internal energy variation, this term can be split according to the variation of the primary fields as:

$$\delta\Pi_{int}(\mathbf{u},\delta\mathbf{u},\phi,\delta\phi) = \delta\Pi^u_{int}(\mathbf{u},\delta\mathbf{u},\phi) + \delta\Pi^\phi_{int}(\mathbf{u},\phi,\delta\phi), \quad \forall\delta\mathbf{u} \in \mathcal{V}_u, \quad \forall\delta\phi \in \mathcal{V}_\phi. \tag{11}$$

Complying with the infinitesimal strain setting as the modeling framework, the weak form of the variation of the internal energy with respect to the displacement field reads as:

$$\delta\Pi^u_{int}(\mathbf{u},\delta\mathbf{u},\phi) = \int_{\mathcal{B}} \boldsymbol{\sigma}(\phi) : \delta\boldsymbol{\varepsilon} \, \mathrm{d}V + \int_{\Gamma_{\mathrm{i}}} \boldsymbol{\tau}(\phi) : \delta\boldsymbol{\Delta} \, \mathrm{d}S, \quad \forall\delta\mathbf{u} \in \mathcal{V}_u \tag{12}$$

where $\boldsymbol{\sigma}(\phi) = \partial_{\boldsymbol{\varepsilon}} \Psi_{\mathrm{b}}$ is the stress tensor which depends on the phase field variable via the so-called degradation function $g(\phi) = (1-\phi)^2$ and $\delta\boldsymbol{\varepsilon} = \partial_{\mathbf{u}}\boldsymbol{\varepsilon}(\delta\mathbf{u})$ is the variation of the strain tensor $\boldsymbol{\varepsilon}$; both are associated to the bulk region. Similarly, $\boldsymbol{\tau}(\phi) = \partial_{\boldsymbol{\Delta}} \Psi_{\mathrm{i}}$ is the cohesive tractions and $\delta\boldsymbol{\Delta} = \partial_{\mathbf{u}}\boldsymbol{\Delta}(\delta\mathbf{u})$ is the variation of the displacement jumps; both are associated with the interface region. It is worth noting that both stress tensors, $\boldsymbol{\sigma}$ and $\boldsymbol{\tau}$, formally depend on the displacement and phase fields as is denoted in the corresponding terms.

In a similar way, the weak form resulting from the variation of the internal energy with respect to the phase field renders

$$\delta\Pi^\phi_{int}(\mathbf{u},\phi,\delta\phi) = \int_{\mathcal{B}} \left[\mathcal{F}_b \delta\phi + \frac{\mathcal{G}_c}{\ell} \left(\phi\delta\phi + \nabla(\delta\phi) \cdot \boldsymbol{\mathcal{L}} \nabla\phi \right) \right] \mathrm{d}V + \int_{\Gamma_{\mathrm{i}}} \mathcal{F}_i \delta\phi \, \mathrm{d}S, \quad \forall\delta\phi \in \mathcal{V}_\phi \tag{13}$$

where $\mathcal{F}_b = \partial_\phi \Psi_{\rm b} = -2(1-\phi)\Psi_{\rm act}$ and $\mathcal{F}_i = \partial_\phi \Psi_{\rm i}$ stand for the bulk and the interface contributions to the energetic force that drives the phase field evolution, respectively. Note that $\mathcal{F}_b$ is obtained assuming the active-passive energy decomposition defined in Eq. (9). After some algebraic manipulations, the variation of the coupled functional associated with the phase field contribution can be rewritten as:

$$\delta\Pi^{\phi}_{int}(\mathbf{u},\phi,\delta\phi) = \frac{\mathcal{G}_c}{\ell}\int_{\mathcal{B}} \left[(\phi - 2(1-\phi)\mathcal{H})\,\delta\phi + \nabla(\delta\phi)\cdot\boldsymbol{\mathcal{L}}\nabla\phi\right]\,\mathrm{d}V + \int_{\Gamma_{\rm i}} \mathcal{F}_i\delta\phi\,\mathrm{d}S, \quad \forall\delta\phi\in\mathcal{V}_\phi \tag{14}$$

For isotropic crack density surfaces, the fracture toughness $\mathcal{G}_{\rm c}$ is a constant value, and therefore the corresponding expression can be evaluated without any further assumptions. Otherwise, for anisotropic crack density surfaces, $\mathcal{G}_{\rm c}$ represents the nominal fracture toughness accounting for the current local mixed-mode opening. At present, a particular expression for the evaluation of $\mathcal{G}_{\rm c}$ for mixed-mode fracture conditions is not available and requires further research, which is a matter beyond the scope of the current study. In addition, although this is still an open issue within the context of the PF method, assuming a constant value of $\mathcal{G}_{\rm c}$ yields to predictions with very good accuracy in comparison with the experimental data as will be reported in forthcoming sections.

In Eq. (14), $\mathcal{H}$ is a field variable that accounts for the historical value of the crack driving state function $\tilde{\mathcal{D}}$ by setting:

$$\mathcal{H} = \max_{s\in\{0,t\}}\left(\tilde{\mathcal{D}}^s\right) \quad \text{with} \quad \tilde{\mathcal{D}}^s = \frac{\Psi^s_{\rm act}}{\mathcal{G}_c/\ell} \tag{15}$$

where s represents the fully story process and t is the current time step. Thus, this history field ensures two conditions required to correctly model the evolution of a crack: (i) the irreversible condition preventing healing effects and (ii) the positiveness of the crack driving force enforcing for fracture growth. In addition, following Miehe et al [29], the dimensionless character of the crack driving force allows an elastic behavior up to the onset of the failure to be included by setting a threshold $\tilde{\mathcal{D}}^s = \langle \Psi^s_{\rm act}\ell/\mathcal{G}_c - 1\rangle_+$.

Finally, the external energy variation can be written, in its most general form, as:

$$\delta\Pi_{ext}(\mathbf{u},\delta\mathbf{u}) = \int_{\mathcal{B}} \boldsymbol{b}\cdot\delta\mathbf{u}\,\mathrm{d}V + \int_{\partial\mathcal{B}_u}\bar{\boldsymbol{t}}\cdot\delta\mathbf{u}\,\mathrm{d}S \tag{16}$$

2.3. Discrete form

The finite element method (FEM) is used in the current work to solve the displacement-phase coupled field problem. The interpolation of the continuum variables at the element level is performed in the isoparametric space using the first-order Lagrangian shape functions. In this sense, the interpolation operator $\boldsymbol{\mathcal{N}}$ is defined as a matrix arranging the $\mathcal{C}^0$-continuous shape functions, $\mathcal{N}^I$ giving the required support to the node I of the element. It must be pointed out that this operator can have a different expression depending on the region and primary field.

In accordance with the isoparametric concept within FEM, firstly introduced by Irons [56], the spatial approximation and the semi-discrete version of the residual vectors and consistent tangent matrices of the two primary fields ($\mathbf{u}$, ϕ) are presented in the following.

2.3.1. Bulk region

The displacement and phase fields ($\mathbf{u}$, ϕ), as well as their variations ($\delta\mathbf{u}$, $\delta\phi$) and their spatial gradients ($\nabla\mathbf{u}$, $\nabla\phi$) are approximated at the element level as follows:

$$\mathbf{u}\approx\boldsymbol{\mathcal{N}}\mathbf{d}, \quad \delta\mathbf{u}\approx\boldsymbol{\mathcal{N}}\delta\mathbf{d}, \quad \nabla\mathbf{u}\approx\mathbf{B}_{\rm d}\mathbf{d} \tag{17}$$

$$\phi\approx\boldsymbol{\mathcal{N}}_{\mathfrak{d}}\boldsymbol{\mathfrak{d}}, \quad \delta\phi\approx\boldsymbol{\mathcal{N}}_{\mathfrak{d}}\delta\boldsymbol{\mathfrak{d}}, \quad \nabla\phi\approx\mathbf{B}_{\mathfrak{d}}\boldsymbol{\mathfrak{d}} \tag{18}$$

where $\mathbf{d}$ and $\mathfrak{d}$ are the vectors arranging the nodal values of the displacement and phase fields, respectively. In turn, $\mathbf{B}_{\mathrm{d}}$ is the strain-displacement kinematic operator and $\mathbf{B}_{\mathfrak{d}}$ is the compatibility operator with the spatial derivatives of the shape functions corresponding to the phase field variable. As the particular expressions of these operators can be found in Msekh et al. [57], they are omitted here for the sake of brevity.

2.3.2. Interface region

Complying with the formulation of an interface element, the displacement jumps vector ($\boldsymbol{\Delta}$) is expressed in the local frame across the interface [58, 6, 53]. Therefore, the interpolation of $\boldsymbol{\Delta}$ and its variation with respect to the displacement field ($\delta\boldsymbol{\Delta}$) can be expressed at the element level as:

$$\boldsymbol{\Delta} \approx \mathbf{B}_{\Delta}\mathbf{d}, \quad \delta\Delta \approx \mathbf{B}_{\Delta}\delta\mathbf{d} \tag{19}$$

where $\mathbf{B}_{\Delta} = \mathbf{R}(\mathbf{d})\boldsymbol{\mathcal{N}}_{\Delta}\mathbf{L}$ is the kinematic jump-displacement operator that approximates the nodal displacement jump into the integration points of the middle plane of the interface. Here, $\mathbf{L}$ provides the difference between the displacements of the upper and the lower interface points and $\mathbf{R}(\mathbf{d})$ rotates the integration point value from the global to the local frame. Since $\mathbf{R}$ depends on $\mathbf{d}$, this aspect induces a geometric contribution in both the residual vector of the internal forces and the consistent tangent matrix, those cases with large displacements should be accounted for [58]. Taking into account that for a small displacement regime the geometric contribution can be neglected, in the current investigation, this effect has not been considered to approximate the variation of the displacement jumps.

The phase field across the interface is defined as the averaged value between the two homologous points of the upper and bottom interface boundaries, i.e. $\hat{\phi} = (\phi^{+} + \phi^{-})/2$ [41]. Hence, the approximation of the phase field (ϕ) and its variation ($\delta\phi$) at the element level is given by

$$\phi \approx \hat{\mathbf{B}}_{\mathfrak{d}}\boldsymbol{\mathfrak{d}}, \quad \delta\phi \approx \hat{\mathbf{B}}_{\mathfrak{d}}\delta\boldsymbol{\mathfrak{d}} \tag{20}$$

where $\hat{\mathbf{B}}_{\mathfrak{d}} = \boldsymbol{\mathcal{N}}_{\hat{\phi}}\mathbf{M}$ is a compatibility operator of the averaged phase field in which $\mathbf{M}$ is the average operator. More details about the geometrical contribution as well as the particular form of the above operators can be found in [58, 59].

2.3.3. FE residual vectors

The discrete version of the residual vectors of the displacement and phase fields are defined as:

$$\mathbf{R}_{\mathrm{d}}^{int} = \int_{\mathcal{B}} \mathbf{B}_{\mathrm{d}}^{\mathrm{T}}\boldsymbol{\sigma}(\phi)\,\mathrm{d}V + \int_{\Gamma_{\mathrm{i}}} \mathbf{B}_{\Delta}^{\mathrm{T}}\boldsymbol{\tau}(\phi)\,\mathrm{d}S \tag{21}$$

$$\mathbf{R}_{\mathfrak{d}} = \frac{\mathcal{G}_c}{\ell}\int_{\mathcal{B}} \left[(\mathfrak{d} - 2(1-\mathfrak{d})\mathcal{H})\boldsymbol{\mathcal{N}}_{\mathfrak{d}} + \mathbf{B}_{\mathfrak{d}}^{\mathrm{T}}\boldsymbol{\mathcal{L}}\nabla\mathfrak{d}\right]\,\mathrm{d}V + \int_{\Gamma_{\mathrm{i}}} \hat{\mathbf{B}}_{\mathfrak{d}}^{\mathrm{T}}\mathcal{F}_i\,\mathrm{d}S \tag{22}$$

In the first expression, $\mathbf{R}_{\mathrm{d}}^{int}$ stands for the contribution of the internal forces in the out-of-balance force residual of the displacement field. The complete expression including the contribution of body forces and external traction, is given by

$$\mathbf{R}_{\mathrm{d}} = \mathbf{R}_{\mathrm{d}}^{int} - \int_{\mathcal{B}} \boldsymbol{\mathcal{N}}^{\mathrm{T}}\boldsymbol{b}\,\mathrm{d}V - \int_{\partial\mathcal{B}_t} \boldsymbol{\mathcal{N}}^{\mathrm{T}}\bar{\boldsymbol{t}}\,\mathrm{d}S \tag{23}$$

2.3.4. FE consistent tangent matrices

The consistent tangent matrices can be obtained by differentiating the residual vectors with respect to the increment of the primary fields:

$$\mathbf{K}_{\mathrm{dd}} = \int_{\mathcal{B}} \mathbf{B}_{\mathrm{d}}^{\mathrm{T}} \mathbb{C}(\phi) \mathbf{B}_{\mathrm{d}} \, \mathrm{d}V + \int_{\Gamma_{\mathrm{i}}} \mathbf{B}_{\Delta}^{\mathrm{T}} \mathbb{D}(\phi) \mathbf{B}_{\Delta} \, \mathrm{d}S \tag{24}$$

$$\mathbf{K}_{\mathfrak{d}\mathfrak{d}} = \frac{\mathcal{G}_c}{\ell} \int_{\mathcal{B}} \left[((1+2\mathfrak{d})\mathcal{H}) \boldsymbol{\mathcal{N}}_{\mathfrak{d}}^{\mathrm{T}} \boldsymbol{\mathcal{N}}_{\mathfrak{d}} + \mathbf{B}_{\mathfrak{d}}^{\mathrm{T}} \boldsymbol{\mathcal{L}} \mathbf{B}_{\mathfrak{d}} \right] \, \mathrm{d}V + \int_{\Gamma_{\mathrm{i}}} \hat{\mathbf{B}}_{\mathfrak{d}}^{\mathrm{T}} \mathbf{F} \hat{\mathbf{B}}_{\mathfrak{d}} \, \mathrm{d}S \tag{25}$$

where $\mathbb{C} = \partial_{\boldsymbol{\varepsilon}} \boldsymbol{\sigma}$ and $\mathbb{D} = \partial_{\boldsymbol{\Delta}} \boldsymbol{\tau}$ are the nominal tangent operators of the bulk material and cohesive zone model, respectively. In turn, $\mathbf{F} = \partial_{\phi} \mathcal{F}_i$ is the tangent operator of the phase field driving force across the interface with respect to the average phase field. Finally, the coupling matrices $\mathbf{K}_{\mathfrak{d}\mathrm{d}}$ and $\mathbf{K}_{\mathrm{d}\mathfrak{d}}$ are not derived here because they are not necessary for the staggered solution scheme used in the numerical examples. It is worth mentioning that the adoption of a staggered incremental-iterative scheme in conjunction with the Newton–Raphson method is herewith adopted due to its robustness, being of especial interest in the current investigation where several energy dissipation mechanisms can evolve simultaneously.

Remark 1. In the current approach the nominal tangent operators ($\mathbb{C}$, $\mathbb{D}$ and $\mathbf{F}$) are computed using the Complex-Step Derivative Approximation (CSDA) [60], which is briefly summarized in Appendix B. This approach is used with the aim of increasing the robustness in the face of the perturbation parameter, not the accuracy of the approximation. In this sense, CSDA approximates the derivate at $\mathcal{O}(x^2)$ like the classical perturbation step approximation which is used, for instance, in [61, 47].

3. Constitutive material models

3.1. Bulk model

The constitutive model used to model the anisotropic behavior characteristic of LFRCs reproduces the formulation proposed by Quintanas-Corominas et al. [40], and which is summarized in the sequel. Accordingly, the complementary Gibbs free energy Ψ^*, which is the dual form of the Helmholtz free energy, for long fiber composite material can be expressed as (see [2, 28] for a more comprehensive treatment):

$$\Psi(\boldsymbol{\varepsilon}) = \Psi^*(\tilde{\boldsymbol{\sigma}}) = \frac{1}{2} \left(\frac{(\tilde{\sigma}_{\mathrm{L}})^2 - 4\nu_{12}\tilde{\sigma}_{\mathrm{L}}\tilde{p}_{\mathrm{T}}}{E_{11}} + \frac{(\tilde{p}_{\mathrm{T}})^2}{E_T} + \frac{(\tilde{\tau}_{\mathrm{T}})^2}{G_T} + \frac{(\tilde{\tau}_{\mathrm{L}})^2}{G_{12}} \right) \tag{26}$$

where $\tilde{\sigma}_{\mathrm{L}}$, $\tilde{p}_{\mathrm{T}}$, $\tilde{\tau}_{\mathrm{L}}$ and $\tilde{\tau}_{\mathrm{T}}$ identify the effective stress quantities, whose definitions are given by

$$\tilde{\sigma}_{\mathrm{L}} = \tilde{\sigma}_{11}, \quad \tilde{p}_{\mathrm{T}} = \frac{\tilde{\sigma}_{22} + \tilde{\sigma}_{33}}{2}, \quad \tilde{\tau}_{\mathrm{L}} = \sqrt{(\tilde{\sigma}_{12})^2 + (\tilde{\sigma}_{13})^2} \quad \text{and} \quad \tilde{\tau}_{\mathrm{T}} = \frac{1}{2}\sqrt{(\tilde{\sigma}_{22} - \tilde{\sigma}_{33})^2 + 4(\tilde{\sigma}_{23})^2}, \tag{27}$$

where E_{11} is the Young's modulus along the fiber direction, ν_{12} stands for the longitudinal Poisson's coefficient, G_{12} is the shear modulus and E_T and G_T are the transverse and shear modulus:

$$E_T = \frac{E_{22}}{2(1-\nu_{23})} \quad \text{and} \quad G_T = \frac{E_{22}}{2(1+\nu_{23})}, \tag{28}$$

where E_{22} is the Young's modulus in-plane transverse to the fiber direction and ν_{23} denotes the transverse Poisson's coefficient.

Recalling the modeling hypotheses of [40], the degradation of the specific bulk energy for fiber reinforced composites within the context of the PF approach is given by

$$\Psi^*(\tilde{\boldsymbol{\sigma}},\phi) = \left((1-\phi)^2+\eta_\ell\right)\Psi^*_{\text{act}}(\tilde{\boldsymbol{\sigma}}) + \Psi^*_{\text{pas}}(\tilde{\boldsymbol{\sigma}}) \tag{29}$$

being

$$\Psi^*_{\text{act}}(\tilde{\boldsymbol{\sigma}}) = \frac{1}{2}\left(\frac{\left\langle(\tilde{\sigma}_{\text{L}})^2 - 4\nu_{12}\tilde{\sigma}_{\text{L}}\tilde{p}_{\text{T}}\right\rangle_+}{E_{11}} + \frac{\langle\tilde{p}_{\text{T}}\rangle_+^2}{E_T} + \frac{(\tilde{\tau}_{\text{T}})^2}{G_T} + \frac{(\tilde{\tau}_{\text{L}})^2}{G_{12}}\right) \tag{30}$$

$$\Psi^*_{\text{pas}}(\tilde{\boldsymbol{\sigma}}) = \frac{1}{2}\left(\frac{\left\langle(\tilde{\sigma}_{\text{L}})^2 - 4\nu_{12}\tilde{\sigma}_{\text{L}}\tilde{p}_{\text{T}}\right\rangle_-}{E_{11}} + \frac{\langle\tilde{p}_{\text{T}}\rangle_-^2}{E_T}\right) \tag{31}$$

Then, the effective compliance tensor in compact notation $\tilde{\mathbf{H}}$ (vector form) reads

$$\tilde{\mathbf{H}} = \left[\frac{\partial^2\Psi^*}{\partial\tilde{\boldsymbol{\sigma}}\otimes\partial\tilde{\boldsymbol{\sigma}}}\right] = \begin{bmatrix} \frac{1}{E_{11}} & -\frac{v_{12}}{E_{11}} & -\frac{v_{12}}{E_{11}} & 0 & 0 & 0 \\ & \frac{1}{4}(\frac{1}{E_T}+\frac{1}{G_T}) & \frac{1}{4}(\frac{1}{E_T}-\frac{1}{G_T}) & 0 & 0 & 0 \\ & & \frac{1}{4}(\frac{1}{E_T}+\frac{1}{G_T}) & 0 & 0 & 0 \\ & & & \frac{1}{G_T} & 0 & 0 \\ & sym. & & & \frac{1}{G_{12}} & 0 \\ & & & & & \frac{1}{G_{12}} \end{bmatrix} \tag{32}$$

Based on the previous definitions, it is worth mentioning that the crack driving state function can be associated with four different material directions that are in turn related to the following intralaminar damage mechanisms: (11) fiber failure, (22/33) matrix failure, (12/13) shear in-plane and (23) transversal shear failures. See Quintanas-Corominas et al. [40] for further details.

3.2. Interface model

The constitutive model herein envisaged for the interface region is based on the formulation proposed by Turon et al. (TM) [53, 8, 47]. The principal differences of this interface formulation with respect to that proposed by Paggi and Reinoso (PRM) [41] are: (*i*) the post-peak behavior, (*ii*) the mixed-mode interaction, and (*iii*) the initiation criteria. Thus, while a cut-off upon failure is defined in the PRM, the TM sets a softening law after reaching the maximum strength of the interface. Therefore, the PRM can be conceived as a more suitable model for interfaces with moderately low fracture process zones, whereas the TM is inherently formulated to capture the response of cohesive interfaces. Regarding the propagation criterion under mixed-mode interaction, on the one hand, PRM used a standard quadratic one whereas, on the other hand, TM employed the Benzeggagh and Kenane criterion [62].

Taking into account the aforementioned characteristics of the TM formulation, the coupling strategy between the PF and CZM proposed herein differs from the one in the PRM. The current strategy assumes that the damage state in the fracture process zone of a crack originated in the bulk region can induce damage in the interface resulting in a loss of stiffness. Considering that the PF variable and the damage state of the TM formulation represent the ratio of a cracked area at a material point, the coupling between both approaches is performed through the integrity function $m(\boldsymbol{\Delta},\phi)$. In particular, this coupling function has to be a continuous monotonically decreasing function defined between 1 (pristine material) and 0 (fully damaged material). In a general manner, the coupling strategy herein proposed is expressed in terms of the integrity functions associated with the displacement jump and PF fields, i.e. $m_\Delta(\boldsymbol{\Delta})$ and $m_\phi(\phi)$, respectively. Assuming a complementary effect in the stiffness loss, the coupling function proposed for the current framework is:

$$m\left(\boldsymbol{\Delta},\phi\right) \equiv m\left(m_\Delta, m_\phi\right) = m_\Delta m_\phi \tag{33}$$

where m_Δ is computed according to the TM formulation (see Algorithm 1) and m_ϕ to the following evolution law:

$$m_\phi = (1 - r_\phi)^2 \tag{34}$$

where r_ϕ is the PF damage threshold that is integrated over the time t satisfying Kuhn-Tucker conditions as:

$$\text{Activation function:} \quad F_\phi = H_\phi - r_\phi \tag{35}$$

$$\text{Loading function:} \quad H_\phi = \begin{cases} 0 & \text{if} \quad \phi \leq \phi_{\min} \\ \frac{\phi - \phi_{\min}}{\phi_{\max} - \phi_{\min}} & \text{if} \quad \phi_{\min} < \phi < \phi_{\max} \\ 1 & \text{if} \quad \phi \geq \phi_{\max} \end{cases} \tag{36}$$

$$\text{Temporal integration:} \quad r_\phi = \max_{s \in \{0,t\}} \left[H_\phi^s \right] \tag{37}$$

where ϕ is the averaged PF value at the integration point according to the interface element formulation presented in Section 2.3.

As can be appreciated in the previous expression, two limits, $\phi_{\min}$ and $\phi_{\max}$, control the initiation and finalization of the coupling. By setting $\phi_{\min} > 0$, the degradation of the interface properties due to the cracking of the bulk region is delayed which, in turn, precludes the driving of the PF from the very beginning of the analysis. On the other hand, an upper limit for the coupling is established by setting $\phi_{\max} < 1$. Moreover, it is also possible to model a brittle behavior of the interface due to the stiffness loss in the bulk region by setting $\phi_{\min} \approx \phi_{\max}$.

Remark 2. As described in Section 2.3, the quantities of the primary fields are extrapolated into the mid-plane of the interface region through an interface element technology. Hence, in the current approach, ϕ governing the interface constitutive model is the averaged quantity at the mid-plane of the interface region.

To illustrate the behavior associated to the proposed coupling, the equivalent cohesive traction is shown in Figure 2 for an interface with the properties listed in Table 1 and $\phi_{\min} = 0.2$ and $\phi_{\min} = 0.8$ as coupling limits. The colored lines in Figure 2b-c illustrates the degradation of the stiffness as the PF increases, whereas the black line corresponds to the loading cycle depicted in Figure 2a. This cycle combines steps in which the opening of the interface increases and the PF is kept fixed (A, C, and E), with others of in which the opening is kept fixed and the PF increase (B and D). In the following, the black curve behavior is analyzed in terms of the cohesive traction τ, mixed-mode equivalent opening λ and PF ϕ. In step A, the cohesive traction increases according to the effective penalty stiffness due to the opening of the interface. Then, in step B, the traction remains constant until the PF reaches the bottom limit $\phi_{\min}$, after which the cohesive traction decreases as a consequence of the damage growth. Note that, from the point of view of the traction - opening law, this behavior is similar to a relaxation of the interface. In step C, the cohesive traction increases according to the nominal penalty stiffness until reaching the corresponding critical opening. After this point, the cohesive traction decreases due to the opening of the interface according to a nominal cohesive law which has less available free energy density as consequence of the bulk damage. Moving to step D, the cohesive traction decreases due to the increase of the PF up to the rupture of the interface, which happens when the $\phi > \phi_{\max}$. Finally, in step E, the equivalent opening is increased without any effect on the cohesive tractions, demonstrating the complete rupture of the interface.

The work-flow of the interface model accounting for the coupling between TM and PF is presented in Algorithm 1. Nevertheless, it is worth mentioning that through the coupling herein proposed, the fundamental hypotheses of TM are preserved. Therefore, for situations in which failure processes are confined to the interface, we retrieved previous results obtained with such an interface model. To illustrate this claim, we examine the accuracy of the TM for pure interface failure under mixed-mode fracture conditions in Section 4.2. Moreover, for the sake of brevity, the specific details of the TM are herewith omitted and interested readers are referred to [53, 8, 47].

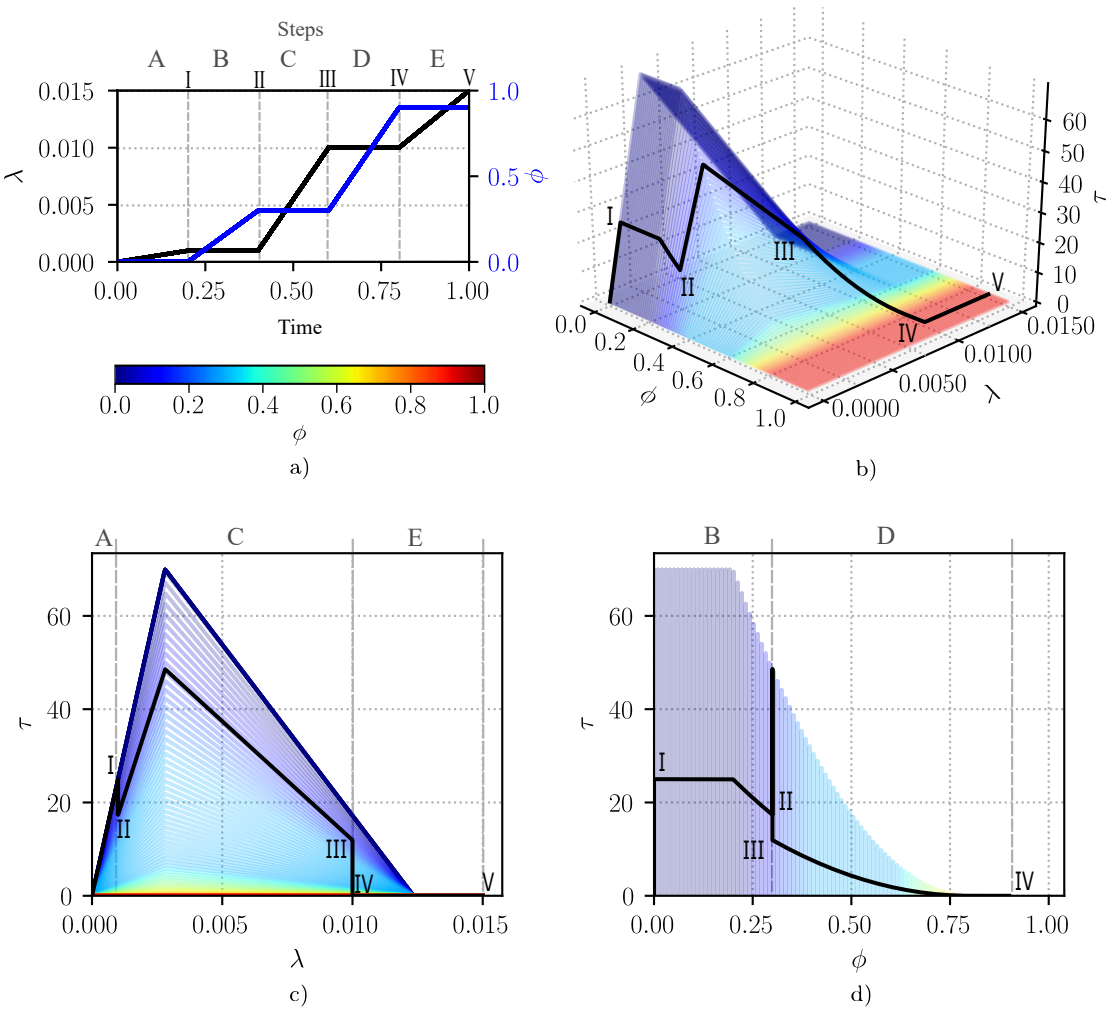

Figure 2: Cohesive traction (τ) behavior for a loading cycle combining equivalent displacement jumps (λ) and phase field (ϕ): a) loading cycle representation b) $\tau - \lambda - \phi$ curves, c) $\tau - \lambda$ and d) $\tau - \phi$. The labels A, B, C and D denote the time interval (step), whereas I, II, III, IV and V a particular instant of time. The black curve in b - d illustrates the response of the loading cycle defined in a. Finally, the rainbow-colored map illustrates the response of the cohesive law for an initial and fixed value of ϕ.

3.2.1. PF driving force and thermodynamic consistency

In this section, we outline the derivations of the PF driving force and the examination of the thermodynamic consistency of the model in the following paragraphs. Recalling the coupling function herein derived, the cohesive interface free energy density function of the TM model can be rewritten as:

$$\Psi_{\mathrm{i}}(\boldsymbol{\Delta}, \phi) = m(\boldsymbol{\Delta}, \phi)\Psi_{\mathrm{i,ela}} \tag{38}$$

where $\Psi_{\mathrm{i,ela}} = (\boldsymbol{\Delta})^{\mathrm{T}}\mathbf{K}\boldsymbol{\Delta}$ is the elastic energy stored in the interface. Here, $\mathbf{K}$ is the elastic stiffness matrix. Note that the dependency of the integrity function with respect to the displacement jumps and PF is here explicitly represented here to emphases the coupling strategy. Then, considering the previous expression and the coupling functions given in Eqs. (33) - (37), the contribution of the interface to the driving force of the PF is defined as:

$$\mathcal{F}_i = \begin{cases} m_\Delta \frac{\partial m_\phi}{\partial r_\phi} \frac{\partial r_\phi}{\partial \phi} \Psi_{\text{i,ela}} & \text{if} \quad 0 < r_\phi < 1 \\ 0 & \text{otherwise} \end{cases} \tag{39}$$

where m_Δ is the integrity function defined in the original TM formulation (see step 9 in Algorithm 1), whereas the partial derivatives accounting for the coupling herein proposed are given by:

$$\frac{\partial m_\phi}{\partial r_\phi} = -2(1 - r_\phi) \tag{40}$$

$$\frac{\partial r_\phi}{\partial \phi} = \frac{1}{(\phi_{\max} - \phi_{\min})} \tag{41}$$

It should be noted that for a fixed displacement jump and, therefore, a fixed m_Δ and $\Psi_{\text{i,ela}}$, the dissipated energy by PF will be the free energy available because of $-\int_0^1 \mathcal{F}_i \mathrm{d}\phi = m_\Delta \Psi_{\text{i,ela}}$.

Algorithm 1 Work-flow for the interface model: cohesive zone model coupled with the phase field approach.

The input material properties are the mode-I and mode-II initial and final jumps (Δ_{Io}, Δ_{IIo}, Δ_{Ic} and Δ_{IIc}) as well as the mode-I and mode-II penalty stiffness (K_{I} and K_{II}). In addition, the Benzeggagh and Kenane parameter η is also given as an input property. It is worth mentioning that Δ_{o} and Δ_{c} can be defined using the fracture toughness and cohesive strength [9]. Here, r_Δ^h and r_ϕ^h are the maximum historical values of the damage threshold variable. Finally, the compact notation is herein used, which means that for a 3D case $\{\boldsymbol{\Delta}\} = \{\Delta_1, \Delta_2, \Delta_3\}^{\text{T}}$ is the displacement jump, $\{\boldsymbol{\tau}\} = \{\tau_1, \tau_2, \tau_3\}^{\text{T}}$ is the tractions and $[\mathbf{K}] = [\mathbf{I}]\{K_{\text{II}}, K_{\text{II}}, K_{\text{I}}\}$ is the penalty stiffness matrix, where $[\mathbf{I}]$ is the identity matrix.

Input: $\{\boldsymbol{\Delta}\}$, ϕ, r_Δ^h, r_ϕ^h, material properties

Output: $\{\boldsymbol{\tau}\}$, $\mathcal{F}_i$, r_Δ, r_ϕ

Compute mixed-mode dependent quantities:

Effective cohesive tractions: $\tilde{\tau} = \sqrt{K_{\text{II}}^2 \Delta_1^2 + K_{\text{II}}^2 \Delta_2^2 + K_{\text{I}}^2 \langle \Delta_3 \rangle_+^2}$

Mixed-mode ratio: $B = (K_{\text{II}} \Delta_1^2 + K_{\text{II}} \Delta_2^2)/(\tilde{\tau})^2$

Equivalent penalty stiffness: $K_B = (1 - B)K_{\text{I}} + BK_{\text{II}}$

Equivalent onset jump: $\lambda_{\text{o}} = \sqrt{(K_{\text{I}} \Delta_{\text{Io}}^2 + (K_{\text{II}} \Delta_{\text{IIo}}^2 - K_{\text{I}} \Delta_{\text{Io}}^2) B^\eta) K_B^{-1}}$

Equivalent critical jump: $\lambda_{\text{c}} = (K_{\text{I}} \Delta_{\text{Io}} \Delta_{\text{Ic}} + (K_{\text{II}} \Delta_{\text{IIo}} \Delta_{\text{IIc}} - K_{\text{I}} \Delta_{\text{Io}} \Delta_{\text{Ic}}) B^\eta)(K_B \lambda_{\text{o}})^{-1}$

Equivalent jump: $\lambda = (K_{\text{II}} \Delta_1^2 + K_{\text{II}} \Delta_2^2 + K_{\text{I}} \langle \Delta_3 \rangle_+^2)(\tilde{\tau})^{-1}$

Compute the integrity function associated to the equivalent jump:

Activation function: $H_\Delta = \min\left[1, \max\left[0, \frac{\lambda - \lambda_{\text{o}}}{\lambda_{\text{c}} - \lambda_{\text{o}}}\right]\right]$

Historical threshold: $r_\Delta = \max\left[r_\Delta^h, H_\Delta\right]$

Integrity function: $m_\Delta = 1 - \frac{r_\Delta \lambda_{\text{c}}}{r_\Delta \lambda_{\text{c}} + (1 - r_\Delta)\lambda_{\text{o}}}$

Compute the integrity function associated to the phase field:

Activation function: $H_\phi = \min\left[1, \max\left[0, \frac{\phi - \phi_{\min}}{\phi_{\max} - \phi_{\min}}\right]\right]$

Historical threshold: $r_\phi = \max\left[r_\phi^h, H_\phi\right]$

Integrity function: $m_\phi = \left(1 - r_\phi\right)^2$

Compute the integrity function according to the coupling function:

Integrity function: $m = \min\left[m_\Delta, m_\phi\right]$

Compute cohesive tractions:

Cohesive tractions: $\{\boldsymbol{\tau}\} = m[\mathbf{K}]\{\boldsymbol{\Delta}\}$

Compute phase field driving force:

Elastic energy: $\Psi_{\text{i,ela}} = \frac{1}{2}\{\boldsymbol{\Delta}\}^T [\mathbf{K}]\{\boldsymbol{\Delta}\}$

Phase field driving force: $\mathcal{F}_i = \begin{cases} m_\Delta \frac{-2(1 - r_\phi)}{\phi_{\max} - \phi_{\min}} \Psi_{\text{i,ela}} & \text{if} \quad 0 < r_\phi < 1 \\ 0 & \text{otherwise} \end{cases}$

4. Numerical treatment and applications

This section briefly introduces the implementation of the proposed formulation in High Performance Computing (HPC) environments, and demonstrates the predictive capabilities in a coupon-based composite specimen.

4.1. HPC implementation and solution scheme

4.1.1. Basic architecture

The proposed model is programmed in the Alya system, which is a multi-physics code conceived for High Performance Computing (HPC) environments, see for instance [4, 63, 64]. This code is written in Fortran 90/95 using a hybrid OpenMP/MPI strategy for efficient parallelization. Thus, the assembly procedure of the right-hand side and the Jacobian matrix do not require communication between nodes. Otherwise, the solution of the algebraic system is performed using built-in iterative solvers and pre-conditioners, which need several communications during the matrix-vector products. In this last case, the MPI gather functions are used, as described by Löhner et al. [65].

4.1.2. Solution scheme

The solution scheme used to compute the numerical predictions of the current coupled displacement-phase field problem is summarized in Algorithm 2. Specifically, the global solution of the coupled problem is obtained via a modified iterative procedure based on the alternate minimization of the two primary fields. The particular modifications from standard staggered solution processes are introduced in the minimization of the PF in order to preclude the necessity of using a bound-constrained optimization solver, which greatly increases the computational costs of the solution procedure.

Moreover, it is worth remarking that the requirement of using these type of solvers arises from the irreversibly condition of the damage evolution imposed in the minimization of the PF in the bulk. Specifically, the strategy herein used is a combination of a posterior projection of the solution used by Lancioni and Royer-Carfagni [66] with a fixation of the solution for values close to 1, which is similar to that employed by Bourdin et al. [15]. In this sense, the solution of PF at the current time step is firstly obtained by solving the unconstrained minimization problem, (step 6). Then, it is imposed that the current solution cannot be smaller than the one at the beginning of the current time step (step 7). Finally, the projected solution of PF is set to 1 wherever it is greater than a threshold value close to 1 (step 8). For the current work, this threshold is considered as 0.95. As pointed out by Amor et al. [54], the posterior projection performed in (step 7) ensures the irreversibly condition of the damage evolution, but it cannot guarantee that the solution found is the global minimum of the constrained problem. However, according to their numerical experiments, there is no significant difference between the results obtained using a bound-constrained optimization solver and the posteriori strategy. Finally, it is worth mentioning that in the related literature, at present, there are alternative solution schemes, such as the so-called over-relaxed alternate minimization proposed by Farrel and Maurini [67] or the primal-dual active set method and predictor-corrector mesh adaptivity used by Heister and coworkers [68], among many others. The numerical performance of these solution schemes with respect to that proposed here, will be a matter of future investigations.

4.2. Verification examples: Mode I and II delamination tests

In this section, two simple simulations are performed to demonstrate that the proposed formulation preserves the original qualities of the cohesive zone model to capture those failure cases driven purely by delamination. The purpose of these tests also encompasses the assessment of the implementation of the cohesive model proposed in [47] in HPC environments. In this sense, the specimen depicted in Figure 3 is simulated considering a Double Cantilever Beam (DCB) configuration as well as an End-Notched Flexural (ENF) one.

Regarding the material, the specimen consists of unidirectional carbon fiber reinforced plies, whose material properties can be found in [47]. The specimen is discretized using a 2D structured mesh conformed by 4-node isoparametric finite elements, which characteristic element size is 0.15x0.13 mm^2 at the bulk

Algorithm 2 Solution scheme: quasi-alternate minimization with posteriori projection.

Let the subscript t and $t-1$ denote the quantities at the current and previous pseudo-time steps along the simulation, respectively. Hence, $(\mathbf{u}_{t-1}, \phi_{t-1})$ is the initial solution of the displacement and the phase field at the begginning of the current time step before applying the Dirichlet-Neumman boundary conditions. Then, $(\mathbf{u}_t, \phi_t)$ is the solution of the primary fields at the current time step, which is evaluated for a fixed tolerance $s_{\max}$ and phase field threshold $\phi_{\text{threshold}}$ with the following iterative procedure:

Input: $\mathbf{u}_{t-1}$, ϕ_{t-1}, $\phi_{\text{threshold}}$, $s_{\max}$
Output: $\mathbf{u}_t$, ϕ_t

Initialize $(\epsilon, p) = (1, 0)$
Set $\left(\mathbf{u}^{(0)}, \phi^{(0)}\right) = (\mathbf{u}_{t-1}, \phi_{t-1})$
While $s \geq s_{\max}$ do
    Increase iteration counter: $p = p + 1$.
    Compute $\mathbf{u}^{(p)}$ by the minimization of $\Pi(\mathbf{u}^{(p-1)}, \phi^{(p-1)})$ subjected to boundary conditions at fixed ϕ .
    Compute $\phi^{(p)}$ by the minimization of $\Pi(\mathbf{u}^{p}, \phi^{(p-1)})$ at fixed $\mathbf{u}$.
    Impose irreversibly condition by setting $\phi^{(p)} = \phi^{(0)}$ wherever $\phi^{(p)} \leq \phi^{(0)}$.
    Impose fully damage condition by setting $\phi^{(p)} = 1$ wherever $\phi^{(p)} \geq \phi_{\text{threshold}}$.
    Compute current residual: $s = \left\|\phi^{(p)} - \phi^{(p-1)}\right\|_{\infty}$.
Set $(\mathbf{u}_t, \phi_t) = \left(\mathbf{u}^{(p)}, \phi^{(p)}\right)$

region and 0.15x0.001 mm^2 at the interface region. This leads to a domain formed by a mesh of 17,350 elements. Finally, the boundary conditions corresponding to each configuration are also illustrated in Figure 3.

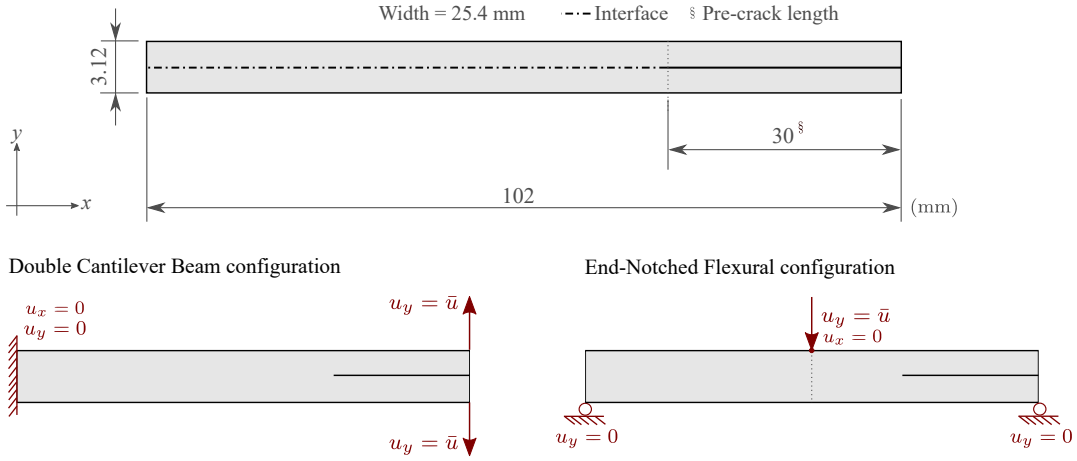

Figure 3: Pure delamination tests: Geometry and boundary conditions for the DCB and ENF configurations.

The load versus displacement curve for the DCB and ENF predicted by the current framework and the Linear Elastic Fracture Mechanics (LEFM) theory are shown in Figure 4. As can be appreciated, both predictions display an excellent agreement with respect to LEFM results. It should be pointed that for this investigation several configurations with different ($\phi_{\min}$,$\phi_{\max}$) have been investigated without any noticeable differences in the corresponding response. In this analysis, the bulk region is not affected by the opening of the interface thanks to the driving force that governs the increase of the PF in the proposed formulation is not affected when the failure is driven purely by a delamination mechanism. Thus, it is expected that the current framework can be used in those cases previously been analyzed with the original CZM.

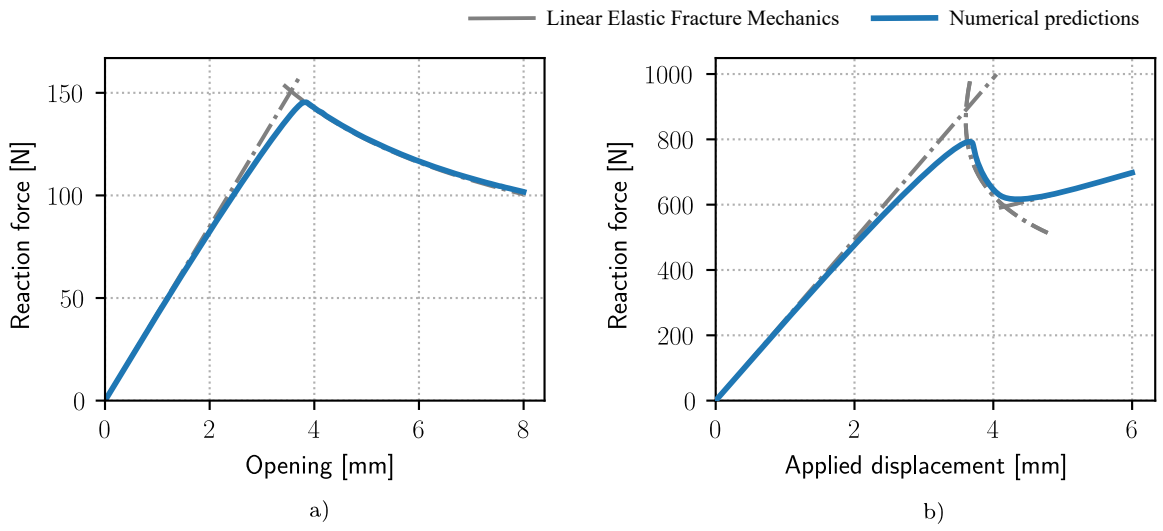

Figure 4: Pure delamination response curves: a) DCB and b) ENF configurations.

4.3. Representative application: 4-Points Bending test

In this section, a four-point bending test is investigated to show the capabilities of the current framework to model the delamination induced by the cracking of the matrix. The specimen considered is a $[90_4/0_7/90_4]$ cross-ply laminate made from HTA/6376 carbon fiber reinforced plies, which was experimentally studied by Mortell et al. [69]. The description of the geometric disposals and dimensions are depicted in Figure 5, while the mechanical properties of the unidirectional ply and interface are listed in Table 1.

Bulk region	E_{11}	140 GPa	Young's modulus (fiber dir.)
	E_{22}	10 GPa	Young's modulus (matrix dir.)
	G_{12}	5.2 GPa	Shear modulus
	ν_{12}	0.3	Poisson ratio
	ν_{13}	0.42	Poisson ratio (isotropy plane)
	Y_T	70 MPa	Tensile transverse strength
	$\xi^\dagger$	1	PF post-peak control parameter
	$\ell_f^\dagger$	1.5	PF length scale (fiber dir.)
	$\ell_m^\dagger$	0.1	PF length scale (matrix dir.)
Interface region	$\tau_I^\dagger$	70 MPa	Cohesive strength: mode-I
	$\tau_{II}^\dagger$	110 MPa	Cohesive strength: mode-II
	$\mathcal{G}_I$	0.432 kJ/m^2	Fracture toughness: mode-I
	$\mathcal{G}_{II}$	1.002 kJ/m^2	Fracture toughness: mode-II
	η	1.75	BK interpolation parameter
	K_I	$1.5{\cdot}10^5$ kN/mm^3	Penalty stiffness: mode-I
	$\phi_{\min}^\dagger$	0.1	PF-CZM coupling limits: min.
	$\phi_{\max}^\dagger$	0.5	PF-CZM coupling limits: max.

† Assumed values.

Table 1: 4PBT material properties and input parameters [69, 70].

Regarding the computational method, the domain is approximated using a 2D structured mesh conformed by 4-node isoparametrical finite elements whose characteristic element size is 0.05 x 0.05 mm^2 at the bulk region and 0.05 x 0.001 mm^2 at the interface. This leads to a mesh of 124,800 elements and 374,400 degrees of freedom. According to the experimental setup, the loading and support conditions can be applied by

modeling the contact between the specimen and steel pins as performed by Reiner et al [70]. However, in the current application, the boundary conditions are applied as point displacements at the positions illustrated in Figure 5. The loading is smoothly applied until a total vertical displacement of $\bar{u} = 6$ mm is reached.

In addition to the aforementioned numerical setup, two more aspects, which are related to the material properties, must be considered:

- The first issue concerns the uniformity of the stress field that takes place along the length between loading pins (span length) due to a constant moment region [69, 70]. From a numerical point of view, this situation provokes the failure onset being able to initiated at any arbitrary location along the span length because the PF will tend to simultaneous and homogeneous growth, only affected by the round-off errors. In turn, this precludes the correct localization of the strain affecting the reliability of the predictions. In this work, this limitation is originally overcome by defining a random field in the finite element mesh affecting only the transverse strength. The correct application of any alternative statistically-based distribution of the corresponding material strength can be considered in forthcoming investigations. Nevertheless, to illustrate this issue of random field by accounting for and complying with the objectives of the current work, a normal distribution with a coefficient of variance of 10% is applied, see Figure 5.

- The second aspect concerns the sensitivity of the delamination onset close to the free-edges. It is wellknown that the mismatch between the Poisson ratios of the plies infers a stress concentration at the interfaces triggering delamination [71]. This issue can be prevented by increasing the fracture toughness of the interface at the regions close to the free-edges as illustrated in Figure 5.

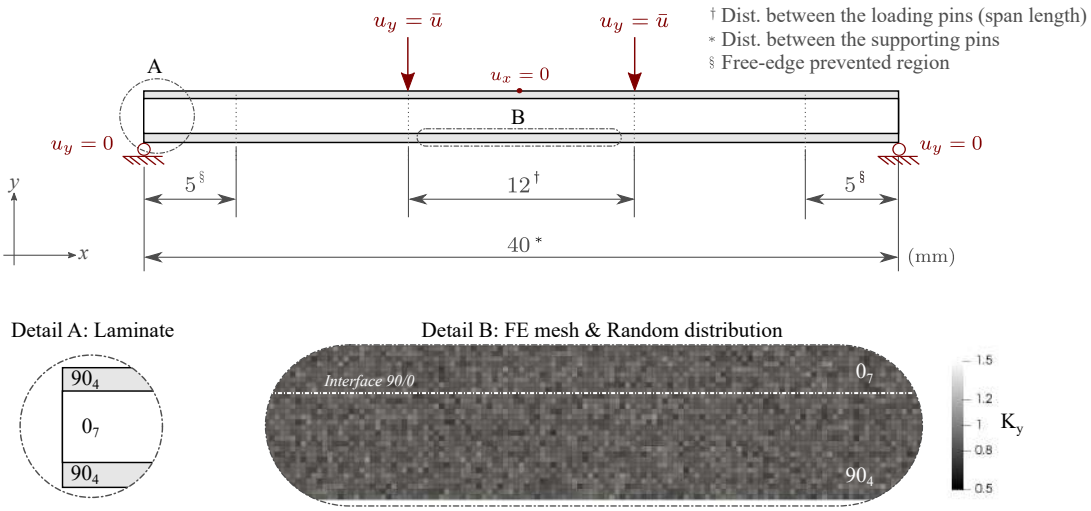

Figure 5: 4PBT scheme: Geometry, boundary conditions and detail of the FE mesh with the random distribution. The nominal strength at the elemental level is defined as $Y_T = K_Y Y_{0,T}$.

As a starting point of the analysis, the need for a coupling strategy between the PF and CZM approaches to capture the delamination induced by matrix cracking is justified. For this purpose, the 4PBT is simulated considering four different FE models, which are listed in Table 2. The fully elastic case is considered here as a reference case, whereas the CZM one is used to illustrate that the delamination is only induced by the transverse cracks. Figure 6.a shows the reaction force at the supports as a function of the applied displacement. From this figure, it can be seen that the curve predicted by the FEM model using only CZM case does not differs from the fully elastic one. Otherwise, a change of slope is predicted by those FE models that use the PF in the bulk region, indicating the onset of transverse cracks.

Focusing on the interaction of a transverse crack when it impinges the interface, it is observed that the delamination onset only occurs in the FE model using the coupling strategy between the PF and CZM, see

Figure 6.b. In the FE model without the coupling strategy, the PF grows parallel to the interface because of the difference in the elastic properties between the 90 and 0 plies. In fact, this mismatch combined with the impossibility of the stresses to relax induces an increase of the PF driving force close to the interface. Moreover, it is noted that without the coupling strategy the crack density is lower than that corresponding to the experimental observations. Therefore, based on this discussion, the coupling strategy becomes a required feature in order to capture the experimental evidence which is characterized by a very complex failure scenario combining intralaminar and interlaminar failure events.

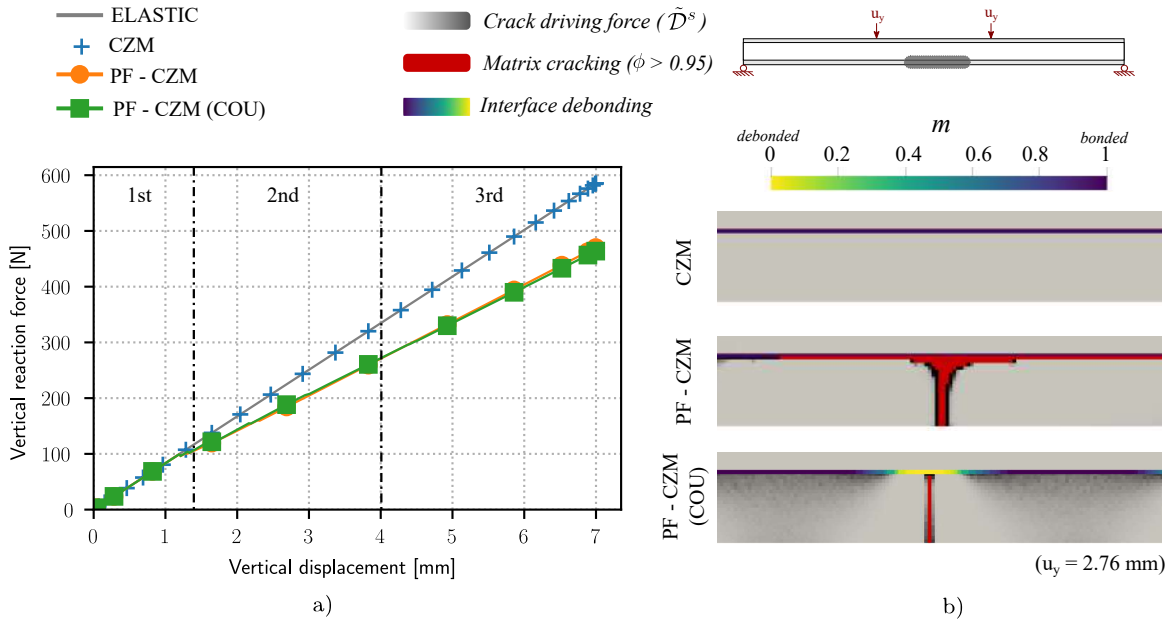

Figure 6: 4PBT results: a) vertical reaction - displacement curve predicted four approaches: (i) elastic, (ii) CZM, (iii) CZM and PF without coupling and (iv) CZM and PF with coupling, b) fracture pattern around a transverse crack for approaches (ii) - (iv). The gray-scale color map illustrates the crack driving force of the transverse cracks, the red color represents fully damaged elements (i.e. wherever $\phi \geq 0.95$) and in the blue-to-yellow colored map the interface debonding in accordance with the integrity function m. Warping scale = 0.

Next, the influence of the $\mathcal{G}_c/\ell$ in Eq. (14) is examined by comparing the stiffness loss in the load direction as a function of the applied displacement for $\mathcal{G}_c/\ell = 0.5, 1, 5, 10, 100$. The normalized curves are plotted in Figure 7.a. Low values of $\mathcal{G}_c/\ell$ induce a more pronounced stiffness loss. This trend is because of the contribution of interface in the driving force of the PF increases as $\mathcal{G}_c/\ell$ decreases affecting the 0 plies. In this sense, if $\mathcal{G}_c/\ell$ is fixed, it plays a role as a scale factor between both contributions: the bulk and interface. To illustrate the affectation of the central plies, the PF across specimen thickness at the location of the first transverse crack is plotted in Figure 7.b. Notice that the PF value in the 0 plies is lower as increases $\mathcal{G}_c/\ell$. Another observation associated with this parameter is related to the onset of the delamination and the crack density. It is observed that the interface debonding takes place prematurely for low values of $\mathcal{G}_c/\ell$. In turn, a relaxation of the stress occurs precluding the onset of new transverse cracks. This observation is shown

Label	Bulk	Interface	Coupling
ELASTIC	elastic	elastic	-
CZM	elastic	CZM	-
PF-CZM	PF	CZM	Off
PF-CZM (COU)	PF	CZM	On

Table 2: 4PBT: FE models considered to justify the coupling strategy.

in Figure 7.c. As can be appreciated, no significant differences regarding the fracture pattern take places for $\mathcal{G}_c/\ell > 5$. Accordingly, in the following, the $\mathcal{G}_c/\ell = 10$ case is analyzed by comparing the numerical predictions against the experimental data.

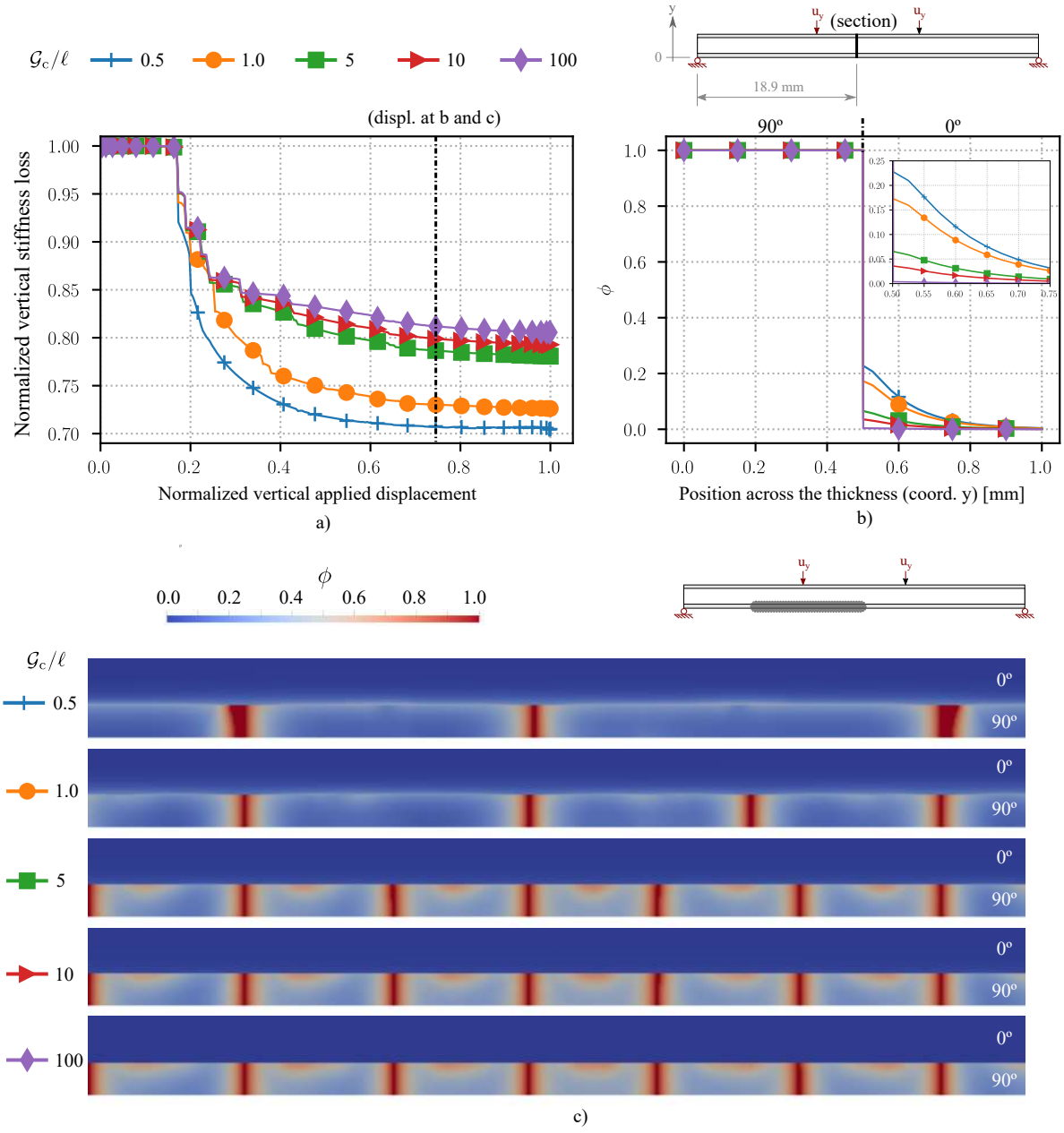

Figure 7: 4PBT results: study of $\mathcal{G}_c/\ell$ influence for $0.5, 1, 5, 10, 100$: a) loss of vertical rigidity - normalized applied displacement, b) PF through the specimen thickness, and c) crack pattern (PF). Warping scale = 0.

Compared with the experimental observations the failure sequence predicted is in agreement with the one reported by Mortell et al. [69]. In the following, the curve predicted by the FE model with the coupling strategy depicted in Figure 6 is taken as guideline with which to compare the results. In the first stage, the curve displays a quasi-elastic evolution up to the onset of the cracking of the bottom plies. The average

stress level at the span length of the outermost ply at first transverse crack initiation predicted (67.5 MPa), which is in close agreement with the experimental findings. Analyzing the failure sequence, the transverse cracking is provoked by a macro-crack that rapidly grows from the bottom edge of the 90 to the 0 plies impinging the 0/90 interface with a micro-delamination, but not reaching the intralamina region of the central 0 plies. After that, in the second stage, the slope of the curve decreases gradually due to the onset of several transverse cracks across the span length. As expected, the new cracks are predicted to be initiated at the center of the span between existing cracks. This is a direct consequence of the fact that it corresponds to the location where the maximum stress occurs since it is outside the free-stress region, see Figure 8. Note also that this relaxed zone is confined in the typical triangular zone [72, 73].

In line with the previous discussion, the number of transverse crack in which the crack length saturates (6 cracks) and the total number of transverse cracks between the supporting pins at the end before the final collapse (14 cracks) are in reasonable agreement with the experimental observations. In addition, the average space between cracks at the end of the simulation (2.25 mm) is close to that recorded in the experiments.

Finally, the third stage commences with the coalescence of the micro-delaminations that debounds the interface which, in turn, triggers the catastrophic collapse of the specimen. Table 3 lists the correlation between the experimental values and the numerical predictions using the proposed PF-CZM coupling method.

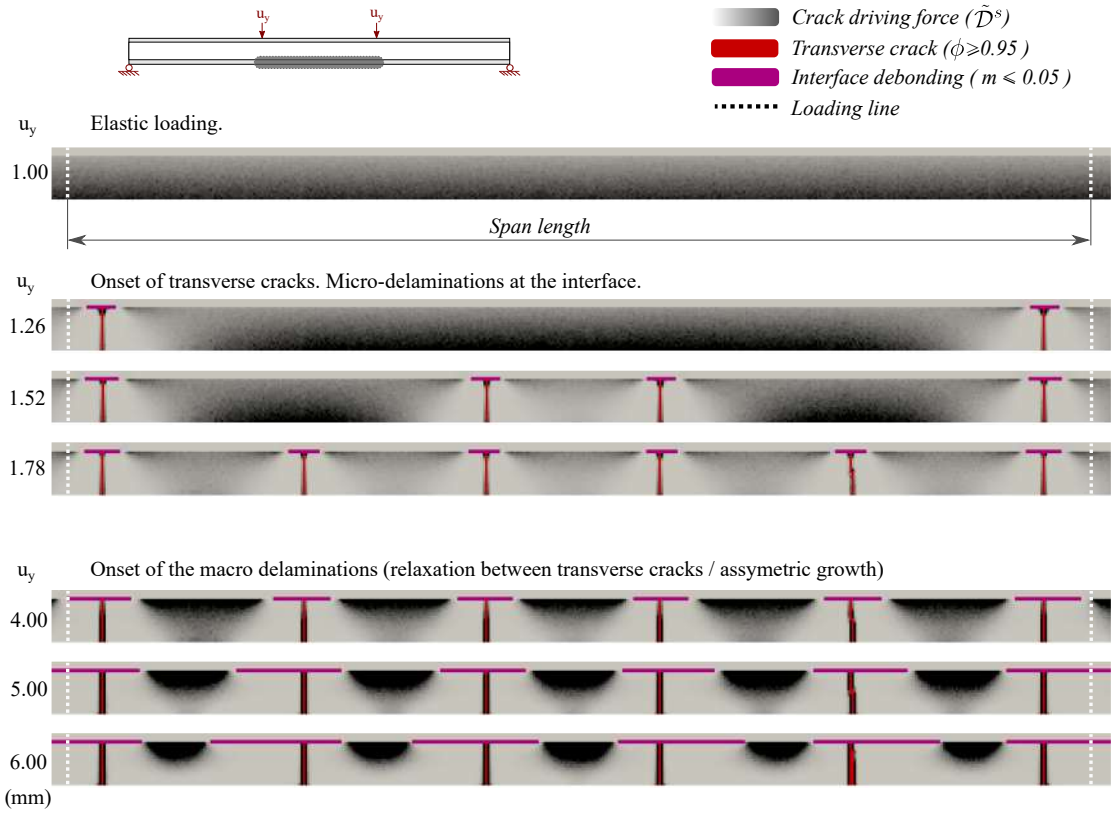

Figure 8: 4PBT results: Fracture pattern of the bottom 90 plies in the span-length region for different applied vertical displacements. The gray-scale color palette illustrates the crack driving force of the transverse cracks, the purple color represents the interface debonding (i.e. wherever $m \leq 0.05$) and the red color represents the transverse cracks (i.e. wherever $\phi \geq 0.95$). Warping scale = 0.

Another interesting phenomenon observed in the experiments is regards delamination growth as as a function of the horizontal location of the transverse crack associated with its triggering. Mortell et al.[69] found that the delamination grows more asymmetrically with respect to the transverse crack far from the center of the specimen than close to it. Moreover, they observed that the preferred direction for the growth

is away from the center of the span length. As can be appreciated in Figure 8 and Figure 9, this behavior has been correctly captured by the current simulations.

Finally, it should be pointed that Mortell et al.[69] also observed that not all the transverse cracks initiate micro-delamination. With the current numerical setup, this behavior is not captured because all transverse cracks damage the interface when they impinge on it. This phenomenon could be modeled by defining a random field for the PF couplings parameters. However, this is not a critical point in the current study.

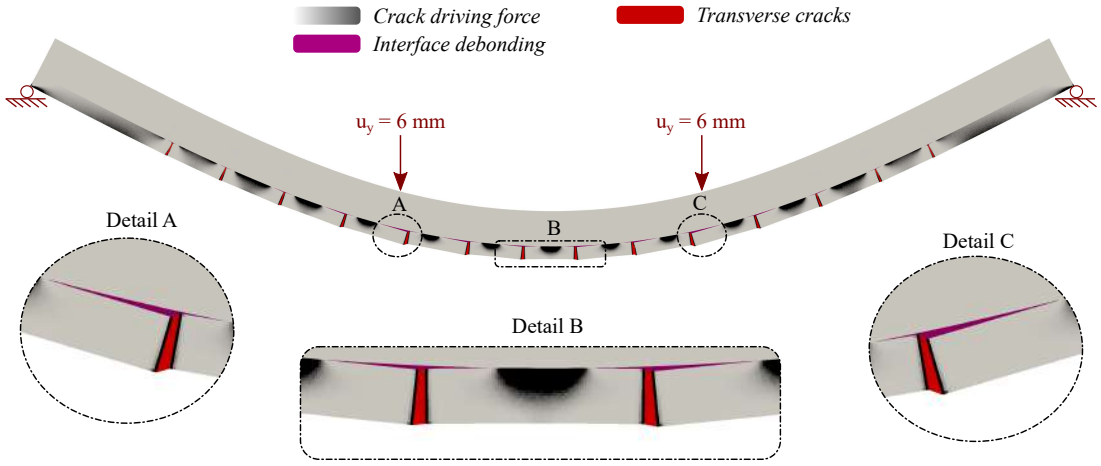

Figure 9: 4PBT results: Fracture pattern for an applied vertical displacement of 6 mm. The gray-scale color map illustrates the crack driving force of the transverse cracks, whereas the red color represents a fully damage elements (i.e. wherever $\phi \geq 0.95$). Warping scale = 1.

5. Conclusions

In the present work, a novel PF-CZM numerical method has been developed to model the delamination induced by matrix cracks in long fiber composite materials.

The current method is characterized by considering the anisotropic PF formulation for the intralaminar damage proposed by Quintanas-Corominas et al. [40], which has been coupled with the cohesive zone model formulation developed by Turon et al. [47]. For this purpose, an alternative coupling strategy between the PF method and the CZM for heterogeneous media with respect to that outlined in [41] has been formulated according to the fundamental aspects of both approaches. In particular, the integrity function of the CZM, which defines the loss of interface rigidity, has been modified, considering of the role of the bulk PF variable in the interface response through the definition of a suitable coupling function. The proposed framework has been implemented in the Alya FE code [64].

Observation	Experimental	Numerical	Units
Onset of the first transverse crack†	62	67.5	MPa
Transverse cracks saturation†	0.7	0.5	crack/mm
Total number of cracks*	15	14	-
Average space between cracks*	2	2.25	mm

† Between the loading pins (span length).
* Between the supporting pins.

Table 3: 4PBT results: Quantitative comparison of the numerical predictions and the experimental observations found by Mortell and co-workers [69, 70].

The capabilities of the proposed formulation have been demonstrated by means of several examples which included the verification of the current interface model in HPC environments and the simulation of a 4-Points Bending Test. The obtained numerical predictions showed that the general trend regarding the failure sequence was correctly captured by the proposed modeling method. Moreover, a direct comparison with experimental observations demonstrated that the proposed framework was also capable of capturing the onset and number of transverse cracks. Finally, the need for a coupling strategy between the CZM and the PF approach to correctly capture the delamination induced by transverse cracking has been shown.

In light of the previous arguments, the formulation herein presented is expected to provide a suitable modeling framework for other engineering problems concerning progressive failure analysis in long fiber composite materials. Future developments might regard the extension of the current framework for performing 3-dimensional simulations of more complex loading scenarios, such as Double-Notched or Open Hole under tensile loading, in conjunction with the incorporation of mesh-adaptive schemes as those proposed in [74, 75] among others, in order to preserve the computational efficiency. In those cases, the approach here presented could be combined with the proposal of Belyer and Alessi [39] to include several phase field variables, achieving a better representation of the different failure mechanisms.

6. Acknowledgments

The Government of Spain has partially funded this work through Ministerio de Educación, Cultura y Deporte under the grant FPU15/06287 and Ministerio de Economia y Competitividad under contracts RTI2018-099373-B-I00 and MAT2015-71036-P. The authors would like to thanks the Red Española de Surpercomputación for giving access to the supercomputer MareNostrum IV based in Barcelona (Spain) through the project FI-2018-3-0022.

Appendix A. Thermodynamic consistency

The thermodynamic consistency of the coupling proposed here is ensured by means of the Clausius-Duhem inequality. Thus, the thermodynamic irreversible condition of the damage process holds if the rate of energy dissipation is positive, i.e.

$$\mathbf{Y} \cdot \dot{\boldsymbol{\mathcal{D}}} \geq 0 \tag{A.1}$$

where $\mathbf{Y}$ is the thermodynamic forces vector conjugated to a set of internal damage variables $\boldsymbol{\mathcal{D}}$ accounting for the dissipative mechanisms. Considering the formulation herein proposed, two internal state variables are defined to measure the damage threshold associated to the displacement and phase fields, which are denoted by r_{Δ} and r_{ϕ}, respectively. It is worth mentioning that the mixed-mode ratio does not affect the damage state as demonstrated by [47] and therefore, it is not considered in the following derivations. Then, the previous inequality can be expressed as:

$$\mathbf{Y} = [-\partial_{m_{\Delta}} \Psi_{\mathrm{i}}, -\partial_{m_{\phi}} \Psi_{\mathrm{i}}]^T \tag{A.2}$$

$$\dot{\boldsymbol{\mathcal{D}}} = [\dot{r}_{\boldsymbol{\Delta}}, \dot{r}_{\phi}] \tag{A.3}$$

which, after some algebraic manipulations, is reduced to

$$-\Psi_{\mathrm{i,ela}} \left(m_{\phi} \frac{\partial m_{\Delta}}{\partial r_{\Delta}} \dot{r}_{\boldsymbol{\Delta}} + m_{\Delta} \frac{\partial m_{\phi}}{\partial r_{\phi}} \dot{r}_{\phi} \right) \geq 0 \tag{A.4}$$

Recalling the demonstration presented by Turon et al. [47] and considering that $m_{\phi} \geq 0$, the first term in the parenthesis is always less than or equal to zero. Hence, the second term should be also less than or equal to zero in order to ensure a positive rate of energy dissipation, i.e.

$$m_\Delta \frac{\partial m_\phi}{\partial r_\phi} \dot{r}_\phi \leq 0 \tag{A.5}$$

where, in light of the expressions summarized in Algorithm 1, it is postulated that

$$m_\Delta = 1 - \frac{r_\mathcal{D}\lambda_\mathrm{c}}{r_\mathcal{D}\lambda_\mathrm{c} + (1 - r_\mathcal{D})\lambda_\mathrm{o}} \geq 0 \tag{A.6}$$

$$\frac{\partial m_\phi}{\partial r_\phi} = -2(1 - r_\phi) \qquad \leq 0 \tag{A.7}$$

At this point, the thermodynamic consistency of the proposed formulation holds thanks to the irreversibly conditions imposed on the damage threshold associated to the phase field variable Eq. (37), i.e. stating that $\dot{r}_\phi \geq 0$.

Appendix B. Complex-step derivative approximation

The Complex-Step Derivative Approximation (CSDA) is used in the current framework to obtain the tangent operator of the material models [60]. When compared to the classical difference approximation, CSDA is more robust than the perturbation parameter h, but it is also more expensive computationally..

Outlining the concept of CSDA, the derivative of a scalar function f can be approximated by perturbing its argument x along the imaginary axis. Thus, the Taylor series expansion of the function around the perturbation is expressed as:

$$f(x + ih) = f(x) + ihf'(x) + \mathcal{O}(x^2) \tag{B.1}$$

where h is the perturbation and $i^2 = -1$ is the imaginary unit number. Then, discarding the high order terms $\mathcal{O}(x^2)$, the first derivative can be approximated as:

$$f'(x) \approx \frac{\mathrm{Im}[f(x + ih)]}{h} \tag{B.2}$$

where $\mathrm{Im}[\bullet]$ is an operator that takes only the imaginary part of the argument. Note that, unlike the traditional method, h can be very small thanks to the above operation is not being subjected to subtractive cancellation [76]. However, the order of the approximation is the same, i.e. $\mathcal{O}(x^2)$.

According to Tanaka and coworkers [77], this concept of CSDA can be extended to directional derivatives of vector fields which, in turn, allows the method for the approximation of the tangent derivative of a material model to be applied. For instance, considering a 2-dimensional analysis and adopting the Voigt notation, the material tangent operator for the bulk region can be explicit represented as:

$$\mathbb{C} = \frac{\partial \boldsymbol{\sigma}}{\partial \boldsymbol{\varepsilon}} \approx \frac{1}{h} \begin{bmatrix} \mathrm{Im}[\sigma_{11}(\boldsymbol{\varepsilon} + ih\tilde{\boldsymbol{\varepsilon}}_{(11)})] & \mathrm{Im}[\sigma_{11}(\boldsymbol{\varepsilon} + ih\tilde{\boldsymbol{\varepsilon}}_{(22)}) & \mathrm{Im}[\sigma_{11}(\boldsymbol{\varepsilon} + ih\tilde{\boldsymbol{\varepsilon}}_{(12)})] \\ \mathrm{Im}[\sigma_{22}(\boldsymbol{\varepsilon} + ih\tilde{\boldsymbol{\varepsilon}}_{(11)})] & \mathrm{Im}[\sigma_{22}(\boldsymbol{\varepsilon} + ih\tilde{\boldsymbol{\varepsilon}}_{(22)}) & \mathrm{Im}[\sigma_{22}(\boldsymbol{\varepsilon} + ih\tilde{\boldsymbol{\varepsilon}}_{(12)})] \\ \mathrm{Im}[\sigma_{12}(\boldsymbol{\varepsilon} + ih\tilde{\boldsymbol{\varepsilon}}_{(11)})] & \mathrm{Im}[\sigma_{12}(\boldsymbol{\varepsilon} + ih\tilde{\boldsymbol{\varepsilon}}_{(22)}) & \mathrm{Im}[\sigma_{12}(\boldsymbol{\varepsilon} + ih\tilde{\boldsymbol{\varepsilon}}_{(12)})] \end{bmatrix} \tag{B.3}$$

where $\tilde{\boldsymbol{\varepsilon}}_{(ij)} = \{\delta_{1(i)}\delta_{1(j)} \quad \delta_{2(i)}\delta_{2(j)} \quad \delta_{1(i)}\delta_{2(j)}\}^T$ is the directional perturbation vectors and δ_{ij} is the Kronecker delta. In turn, the material operator for the cohesive zone model reads as:

$$\mathbb{D} = \frac{\partial \boldsymbol{\tau}}{\partial \boldsymbol{\Delta}} \approx \frac{1}{h} \begin{bmatrix} \mathrm{Im}[\tau_1(\boldsymbol{\Delta} + ih\mathbf{g}_{(11)})] & \mathrm{Im}[\tau_1(\boldsymbol{\Delta} + ih\mathbf{g}_{(22)})] \\ \mathrm{Im}[\tau_2(\boldsymbol{\Delta} + ih\mathbf{g}_{(11)})] & \mathrm{Im}[\tau_2(\boldsymbol{\Delta} + ih\mathbf{g}_{(22)})] \end{bmatrix} \tag{B.4}$$

where $\mathbf{g}_{(ij)} = \{\delta_{1(i)}\delta_{1(j)} \quad \delta_{2(i)}\delta_{2(j)}\}^T$.

References

[1] P. Maimí, P.P. Camanho, J.A. Mayugo, and C.G. Dávila. A continuum damage model for composite laminates: Part I – Constitutive model. *Mechanics of Materials*, 39(10):897 – 908, 2007.

[2] P. Maimí, P.P. Camanho, J.A. Mayugo, and C.G. Dávila. A continuum damage model for composite laminates: Part II – Computational implementation and validation. *Mechanics of Materials*, 39(10):909 – 919, 2007.

[3] J. Reinoso, G. Catalanotti, A. Blázquez, P. Areias, P.P. Camanho, and F. París. A consistent anisotropic damage model for laminated fiber-reinforced composites using the 3d-version of the puck failure criterion. *International Journal of Solids and Structures*, pages 37 – 53, 2017.

[4] A. Quintanas-Corominas, P. Maimí, E. Casoni, A. Turon, J.A. Mayugo, G. Guillamet, and M. Vázquez. A 3D transversally isotropic constitutive model for advanced composites implemented in a high performance computing code. *European Journal of Mechanics - A/Solids*, 71:278 – 291, 2018.

[5] M. Ortiz and A. Pandolfi. Finite deformation irreversible cohesive elements for three-dimensional crack-propagation analysis. *International Journal for Numerical Methods in Engineering*, 44:1267–1282, 1999.

[6] A. Turon, P.P. Camanho, J. Costa, and C.G. Dávila. A damage model for the simulation of delamination in advanced composites under variable-mode loading. *Mechanics of Materials*, 38(11):1072 – 1089, 2006.

[7] P. P. Camanho, C. G. Davila, and M. F. de Moura. Numerical simulation of mixed-mode progressive delamination in composite materials. *Journal of Composite Materials*, 37(16):1415–1438, 2003.

[8] A. Turon, P.P. Camanho, J. Costa, and J. Renart. Accurate simulation of delamination growth under mixed-mode loading using cohesive elements: Definition of interlaminar strengths and elastic stiffness. *Composite Structures*, 92(8):1857 – 1864, 2010.

[9] E.V. González, P. Maimí, J.R. Sainz de Aja, P. Cruz, and P.P. Camanho. Effects of interply hybridization on the damage resistance and tolerance of composite laminates. *Composite Structures*, 108:319 – 331, 2014.

[10] A. Soto, E.V. González, P. Maimí, F. Martín de la Escalera, J.R. Sainz de Aja, and E. Alvarez. Low velocity impact and compression after impact simulation of thin ply laminates. *Composites Part A: Applied Science and Manufacturing*, 109:413 – 427, 2018.

[11] L. Carreras, E. Lindgaard, J. Renart, B.L.V. Bak, and A. Turon. An evaluation of mode-decomposed energy release rates for arbitrarily shaped delamination fronts using cohesive elements. *Computer Methods in Applied Mechanics and Engineering*, 347:218 – 237, 2019.

[12] A. Sasikumar, J. Costa, D. Trias, E.V. González, S.M. García-Rodríguez, and P. Maimí. Unsymmetrical stacking sequences as a novel approach to tailor damage resistance under out-of-plane impact loading. *Composites Science and Technology*, 173:125 – 135, 2019.

[13] R.H.J. Peerlings, M.G.D. Geers, R. De, and W.A.M. Brekelmans. A critical comparison of nonlocal and gradient-enhanced softening continua. *International Journal of solids and Structures*, 38:7723–7746, 2001.

[14] G.A. Francfort and J.-J. Marigo. Revisiting brittle fracture as an energy minimization problem. *Journal of the Mechanics and Physics of Solids*, 46(8):1319 – 1342, 1998.

[15] B. Bourdin, G.A. Francfort, and J.J. Marigo. Numerical experiments in revisited brittle fracture. *Journal of the Mechanics and Physics of Solids*, 48(4):797 – 826, 2000.

[16] B. Bourdin, G.A. Francfort, and J.J. Marigo. The variational approach to fracture. *Journal of Elasticity*, 91(1):5 – 148, 2008.

[17] C. Miehe, F. Welschinger, and M. Hofacker. Thermodynamically consistent phase-field models of fracture: Variational principles and multi-field FE implementations. *International Journal for Numerical Methods in Engineering*, 83(10):1273 – 1311, 2010.

[18] M.J. Borden, C.V. Verhoosel, M.A. Scott, T. Hughes, and C.M. Landis. A phase-field description of dynamic brittle fracture. *Computer Methods in Applied Mechanics and Engineering*, 217-220(8):77 – 95, 2012.

[19] M. Hofacker and C. Miehe. A phase field model of dynamic fracture: Robust field updates for the analysis of complex crack patterns. *International Journal for Numerical Methods in Engineering*, 93:276–301, 2013.

[20] M.F. Wheeler, T. Wick, and W. Wollner. An augmented-lagrangian method for the phase-field approach for pressurized fractures. *Computer Methods in Applied Mechanics and Engineering*, 271:69 – 85, 2014.

[21] J. Reinoso, M. Paggi, and C. Linder. Phase field modeling of brittle fracture for enhanced assumed strain shells at large deformations: formulation and finite element implementation. *Computational Mechanics*, 59(6):981–1001, 2017.

[22] H. Ulmer, M. Hofacker, and C. Miehe. Phase field modeling of brittle and ductile fracture. *PAMM*, 13:533–536, 2013.

[23] M. Ambati, T. Gerasimov, and L. De Lorenzis. Phase-field modeling of ductile fracture. *Computational Mechanics*, 55:1017–1040, 2015.

[24] M. Ambati and L. De Lorenzis. Phase-field modeling of brittle and ductile fracture in shells with isogeometric nurbs-based solid-shell elements. *Computer Methods in Applied Mechanics and Engineering*, 312:351–373, 2016.

[25] R. Alessi, J.J. Marigo, C. Maurini, and S. Vidoli. Coupling damage and plasticity for a phase-field regularisation of brittle, cohesive and ductile fracture: One-dimensional examples. *International Journal of Mechanical Sciences*, 149:559 – 576, 2018.

[26] Z.A. Wilson and C.M. Landis. Phase-field modeling of hydraulic fracture. *Journal of the Mechanics and Physics of Solids*, 96:264 – 290, 2016.

[27] E. Martínez-Pañeda, A. Golahmar, and C.F. Niordson. A phase field formulation for hydrogen assisted cracking. *Computer Methods in Applied Mechanics and Engineering*, 342:742 – 761, 2018.

[28] C. Miehe, L. Schänzel, and H. Ulmer. Phase field modeling of fracture in multi-physics problems. Part I. balance of crack

surface and failure criteria for brittle crack propagation in thermo-elastic solids. *Computer Methods in Applied Mechanics and Engineering*, 294:449 – 485, 2015.

[29] C. Miehe, M. Hofacker, L.-M. Schänzel, and F. Aldakheel. Phase field modeling of fracture in multi-physics problems. Part II. coupled brittle-to-ductile failure criteria and crack propagation in thermo-elastic–plastic solids. *Computer Methods in Applied Mechanics and Engineering*, 294:486 – 522, 2015.

[30] C. Miehe and S. Mauthe. Phase field modeling of fracture in multi-physics problems. part iii. crack driving forces in hydro-poro-elasticity and hydraulic fracturing of fluid-saturated porous media. *Computer Methods in Applied Mechanics and Engineering*, 304:619 – 655, 2016.

[31] B. Li, C. Peco, D. Millán, I. Arias, and M. Arroyo. Phase-field modeling and simulation of fracture in brittle materials with strongly anisotropic surface energy. *International Journal for Numerical Methods in Engineering*, 102:711–727, 2014.

[32] O. Gültekin, H. Dal, and G.A. Holzapfel. A phase-field approach to model fracture of arterial walls: Theory and finite element analysis. *Computer Methods in Applied Mechanics and Engineering*, 312:542 – 566, 2016.

[33] X. Zhang, S.W. Sloan, C. Vignes, and D. Sheng. A modification of the phase-field model for mixed mode crack propagation in rock-like materials. *Computer Methods in Applied Mechanics and Engineering*, 322:123 – 136, 2017.

[34] T. Tung, J. Réthoré, and M.C. Baietto. Phase field modelling of anisotropic crack propagation. *European Journal of Mechanics - A/Solids*, 65:279–288, 2017.

[35] S. Teichtmeister, D. Kienle, F. Aldakheel, and M.A. Keip. Phase field modeling of fracture in anisotropic brittle solids. *International Journal of Non-Linear Mechanics*, 97:1 – 21, 2017.

[36] T.T. Nguyen, J. Réthoré, J. Yvonnet, and M.C. Baietto. Multi-phase-field modeling of anisotropic crack propagation for polycrystalline materials. *Computational Mechanics*, 60(2):289–314, 2017.

[37] E.G. Kakouris and S.P. Triantafyllou. Material point method for crack propagation in anisotropic media: a phase field approach. *Archive of Applied Mechanics*, 88(1):287–316, 2018.

[38] J. Reinoso, A. Arteiro, M. Paggi, and P.P. Camanho. Strength prediction of notched thin ply laminates using finite fracture mechanics and the phase field approach. *Composites Science and Technology*, 150:205 – 216, 2017.

[39] J. Bleyer and R. Alessi. Phase-field modeling of anisotropic brittle fracture including several damage mechanisms. *Computer Methods in Applied Mechanics and Engineering*, 336:213 – 236, 2018.

[40] A. Quintanas-Corominas, J. Reinoso, E. Casoni, A. Turon, and J.A. Mayugo. A phase field approach to simulate intralaminar and translaminar fracture in long fiber composite materials. *Composite Structures*, 2019.

[41] M. Paggi and J. Reinoso. Revisiting the problem of a crack impinging on an interface:a modeling framework for the interaction between the phase field approach for brittle fracture and the interface cohesive zone model. *Computer Methods in Applied Mechanics and Engineering*, 321:145 – 172, 2017.

[42] V. Carollo, J. Reinoso, and M. Paggi. A 3D finite strain model for intralayer and interlayer crack simulation coupling the phase field approach and cohesive zone model. *Composite Structures*, 182:636 – 651, 2017.

[43] V. Carollo, J. Reinoso, and M. Paggi. Modeling complex crack paths in ceramic laminates: a novel variational framework combining the phase field method of fracture and the cohesive zone model. *Journal of the European Ceramic Society*, 38(8):2994–3003, 2018.

[44] M. Paggi, M. Corrado, and J. Reinoso. Fracture of solar-grade anisotropic polycrystalline silicon: A combined phase field–cohesive zone model approach. *Computer Methods in Applied Mechanics and Engineering*, 330:123 – 148, 2018.

[45] T. Guillén-Hernández, I.G. García, J. Reinoso, and M. Paggi. A micromechanical analysis of inter-fiber failure in long reinforced composites based on the phase field approach of fracture combined with the cohesive zone model. *International Journal of Fracture (under revision)*, 2019.

[46] Kumchol Yun, Songhun Kwak, Zhenqing Wang, Mengzhou Chang, Jonggun Kim, Jingbiao Liu, and Cholsu Ri. A damage model reflecting the interaction between delamination and intralaminar crack for failure analysis of frp laminates. *Applied Sciences*, 9(2), 2019.

[47] A. Turon, E.V. González, C. Sarrado, G. Guillamet, and P. Maimí. Accurate simulation of delamination under mixed-mode loading using a cohesive model with a mode-dependent penalty stiffness. *Composite Structures*, 184(10–11):506 – 511, 2018.

[48] T-T Nguyen, J Yvonnet, Q-Z Zhu, M Bornert, and C Chateau. A phase-field method for computational modeling of interfacial damage interacting with crack propagation in realistic microstructures obtained by microtomography. *Computer Methods in Applied Mechanics and Engineering*, 312:567–595, 2016.

[49] T-T Nguyen, J Yvonnet, M Bornert, and C Chateau. Initiation and propagation of complex 3d networks of cracks in heterogeneous quasi-brittle materials: direct comparison between in situ testing-microct experiments and phase field simulations. *Journal of the Mechanics and Physics of Solids*, 95:320–350, 2016.

[50] A. Griffith. The phenomena of rupture and flow in solids. *Philosophical transactions of the royal society of london. Series A, containing papers of a mathematical or physical character*, 221:163 – 198, 1921.

[51] L. Ambrosio and V.M. Tortorelli. Approximation of functional depending on jumps by elliptic functional via t-convergence. *Communications on Pure and Applied Mathematics*, 43(8):999 – 1036, 1990.

[52] J.J. Marigo, M. Corrado, and K. Pahm. An overview of the modelling of fracture by gradient damage models. *Meccanica*, 51(12):3107–3128, 2016.

[53] A. Turon, C.G. Dávila, P.P. Camanho, and J. Costa. An engineering solution for mesh size effects in the simulation of delamination using cohesive zone models. *Engineering Fracture Mechanics*, 74(10):1665 – 1682, 2007.

[54] H. Amor, J.J. Marigo, and C. Maurini. Regularized formulation of the variational brittle fracture with unilateral contact: Numerical experiments. *Journal of the Mechanics and Physics of Solids*, 57:1209–1229, 2009.

[55] T.J.R. Hughes. *The Finite Element Method: Linear Static and Dynamic Finite Element Analysis*. Dover Civil and Mechanical Engineering. Dover Publications, 2000.

[56] B.M. Irons. Engineering applications of numerical integration in stiffness methods. *AIAA Journal*, 11(4):2035—-2037, 1966.
[57] M. Msekh, J.M. Sargado, M. Jamshidian, P. Areias, and T. Rabczuk. Abaqus implementation of phase-field model for brittle fracture. *Computational Materials Science*, 96(12):472 – 484, 2015.
[58] J. Reinoso and M. Paggi. A consistent interface element formulation for geometrical and material nonlinearities. *Computational Mechanics*, 54:1569–1581, 2014.
[59] M. Paggi and J. Reinoso. An anisotropic large displacement cohesive zone model for fibrillar and crazing interfaces. *International Journal of Solids and Structures*, 69:106–120, 2015.
[60] J.R.R.A. Martins, P. Sturdza, and J.J. Alonso. The Complex-step Derivative Approximation. *ACM Trans. Math. Softw.*, 29(3):245–262, 2003.
[61] X. Martínez, S. Oller, F. Rastellini, and A.H. Barbat. A numerical procedure simulating {RC} structures reinforced with {FRP} using the serialparallel mixing theory. *Computers & Structures*, 86:1604–1618, 2008.
[62] M.L. Benzeggagh and M. Kenane. Measurement of mixed-mode delamination fracture toughness of unidirectional glass/epoxy composites with mixed-mode bending apparatus. *Composites Science and Technology*, 56(4):439–449, 1996.
[63] E. Casoni, A. Jérusalem, C. Samaniego, B. Eguzkitza, P. Lafortune, D.D. Tjahjanto, X. Sáez, G. Houzeaux, and M. Vázquez. Alya: Computational solid mechanics for supercomputers. *Archives of Computational Methods in Engineering*, 22:557–576, 2014.
[64] M. Vázquez, G. Houzeaux, S. Koric, A. Artigues, J. Aguado-Sierra, R. Arís, D. Mira, H. Calmet, F. Cucchietti, H. Owen, A. Taha, E. Derin, J.M. Cela, and M. Valero. Alya: Multiphysics engineering simulation toward exascale. *Journal of Computational Science*, 14:15–27, 2016.
[65] R. Löhner, F. Mut, J.R. Cebral, R. Aubry, and G. Houzeaux. Deflated preconditioned conjugate gradient solvers for the pressure-poisson equation: Extensions and improvements. *International Journal for Numerical Methods in Engineering*, 87:2–14, 2011.
[66] G. Lancioni and G. Royer-Carfagni. The Variational Approach to Fracture Mechanics. A Practical Application to the French Panthéon in Paris. *Journal of Elasticity*, 95(1):1–30, 2009.
[67] P. Farrell and C. Maurini. Linear and nonlinear solvers for variational phase-field models of brittle fracture. *International Journal for Numerical Methods in Engineering*, 109(5):648–667, 201.
[68] T. Heister, M.F. Wheeler, and T. Wick. A primal-dual active set method and predictor-corrector mesh adaptivity for computing fracture propagation using a phase-field approach. *Computer Methods in Applied Mechanics and Engineering*, 290:466 – 495, 2015.
[69] D.J. Mortell, D.A. Tanner, and C.T. McCarthy. In-situ sem study of transverse cracking and delamination in laminated composite materials. *Composites Science and Technology*, 105:118 – 126, 2014.
[70] J. Reiner, M. Veidt, M. Dargusch, and L. Gross. A progressive analysis of matrix cracking-induced delamination in composite laminates using an advanced phantom node method. *Journal of Composite Materials*, 51(20):2933 – 2947, 2017.
[71] G. Guillamet, A. Turon, J. Costa, and P. Linde. A quick procedure to predict free-edge delamination in thin-ply laminates under tension. *Engineering Fracture Mechanics*, 168, Part B:28 – 39, 2016.
[72] J.A. Mayugo, P.P. Camanho, P. Maimí, and C.G. Dávila. Analytical modelling of transverse matrix cracking of 0/90ns composite laminates under multiaxial loading. *Mechanics of Advanced Materials and Structures*, 17(4):237 – 245, 2010.
[73] P. Maimí, P.P. Camanho, J.A. Mayugo, and A. Turon. Matrix cracking and delamination in laminated composites. Part I: Ply constitutive law, first ply failure and onset of delamination. *Mechanics of Materials*, 43(4):169 – 185, 2011.
[74] H. Badnava, M.A. Msekh, E. Etemadi, and T. Rabczuk. An h-adaptive thermo-mechanical phase field model for fracture. *Finite Elements in Analysis and Design*, 138(4):31 – 47, 2018.
[75] Hirshikesh, A.L.N. Pramod, R.K. Annabattula, E.T. Ooi, C. Song, and S. Natarajan. Adaptive phase-field modeling of brittle fracture using the scaled boundary finite element method. *Computer Methods in Applied Mechanics and Engineering*, 355:284 – 307, 2019.
[76] S. Kim, J. Ryu, and M. Cho. Numerically generated tangent stiffness matrices using the complex variable derivative method for nonlinear structural analysis. *Computer Methods in Applied Mechanics and Engineering*, 200(1):403 – 413, 2011.
[77] M. Tanaka, M. Fujikawa, D. Balzani, and J. Schr oder. Robust numerical calculation of tangent moduli at finite strains based on complex-step derivative approximation and its application to localization analysis. *Computer Methods in Applied Mechanics and Engineering*, 269:454 – 470, 2014.